Evaluation of welding joint methods for a prismatic battery cell module

William Hellingwerf

DEPARTMENT OF DESIGN SCIENCES
FACULTY OF ENGINEERING LTH | LUND UNIVERSITY
2021

MASTER THESIS

northvolt®

Evaluation of welding joint methods for a prismatic battery cell module

Master Thesis

William Hellingwerf
2021

LUNDS
UNIVERSITET

Evaluation of welding joint methods for a prismatic battery cell module

Master Thesis

Published by
Department of Design Sciences
Faculty of Engineering, Lund University
P.O. Box 118, SE-221 00 Lund, Sweden

Subject: Technical Design (MMKM10)
Supervisor: Per Kristav
Examiner: Axel Nordin

Abstract

Prismatic battery cells swell due to a number of different factors, such as state of charge, temperature and irreversibly with charge cycling. Cell health can be improved by restricting the swelling of the cell, and therefore, the container which holds the cells, the module, should be able to restrict the swelling, and thus withstand the force exerted by the cells.

This paper evaluates the use of three different welding techniques to use with a specified module frame constructed out of aluminium. The welding of the module will be performed with the cells in place and as of safety reasons to avoid the devastating effects of a thermal runaway, a maximum temperature requirement is set on the cell side of the welded parts.

The three welding techniques evaluated in this report are, tungsten inert gas, friction stir, and laser welding. Which are evaluated on a basis of strength and maximum temperature development during the welding process.

This paper focuses on comparing the three different methods relative each other. Calculations and simulations should not in any way be considered accurate or be used for dimensioning without extensive validation.

The most promising welding method in this report is laser welding, as the research points toward a significant safety factor towards the maximum allowed temperatures on the cells. However, the strength requirement is not met with the use of the same alloys as suggested with the other techniques, but is promising with the use of alternative alloys.

Keywords: Aluminium welding methods, Battery module, Prismatic cell, Weld strength, Weld analysis, Weld temperature simulation.

Sammanfattning

Prismatiska battericeller sväller på grund av ett antal olika faktorer, såsom laddningstillstånd och temperatur, men också irreversibelt med laddningscykling. Cellhälsan kan förbättras genom att begränsa svällnad av cellen, och därmed bör konstruktionen som håller cellerna på plats, modulen, kunna begränsa svullnaden och därmed motstå det lastfall som skapas av cellsvällnaden.

Denna uppsats utvärderar användandet av tre olika svetstekniker, med avsikt att användas för att konstruera en batterimodulsram i aluminium för prismatiska celler. Svetsning av modulen sker med cellerna på plats. Därför, av säkerhetsskäl för att undvika att värma upp cellerna till farligt höga temperaturer, ställs ett krav på den maximala temperaturen som mäts upp på cellsidan.

De tre svetsmetoder som utvärderas i denna rapport är TIG svetsning, friktionsrörssvetsning och lasersvetsning. Dessa utvärderas utifrån styrka och maximal temperaturutveckling under svetsprocessen.

Denna uppsats fokuserar på att jämföra de tre olika metoderna relativt verandra. Beräkningar och simuleringar bör inte anses vara sanningsenliga eller användas för dimensionering utan omfattande validering.

Den mest lovande svetsmetoden i denna rapport är lasersvetsning, då resultaten i rapporten pekar mot en signifikant säkerhetsfaktor mot de maximalt tillåtna temperaturerna på cellerna. Däremot uppfylls inte hållfasthetskravet med samma legeringar som föreslagits för de andra metoderna. Däremot kan användandet av andra legeringar öka svetsens hållfasthet.

Nyckelord: Aluminium, Svetsmetoder, Batterimodul, Prismatisk cell, Svetshållfasthet, Svetstemperatursimulering.

Preface/Acknowledgements

There is something special about writing this thesis.

I have for many years known that I wanted to take part in the electrification of transport. During the first year of my studies, I joined the Formula Student team at Lunds Tekniska Högskola (LTH) with the dream of to one day take part in building an electric race car. It was during this first year that I decided that my final masters thesis would be about the electrification of motorcycles. Well. This thesis is not about the electrification of motorcycles, but I would still consider my dreams fulfilled. In the last year of my studies, I took part in designing the first fully electric race car at Lund Formula Student, designing the battery pack together with a small team. And now, I am writing my thesis at northvolt, continuing the path of developing batteries, possibly for use in transportation / automotive industry.

I would like to thank my supervisor Per Kristav at LTH, for his engagement and support in this thesis, and my northvolt supervisor Kenya Shatani, for trusting me in developing my own process and thesis topic. Another thanks goes to Michel Chapuis for his encouragement and for patiently and answering a non-finite amount of questions

And lastly I would like to thank Lund Formula Student, (LFS), in which I have spent three and a half years of my studies. LFS has provided me with many of the skills and most of my confidence as an engineer. It is also responsible for *many many many* sleepless nights, tired eyes but also great friendship.

Contents

List of acronyms and abbreviations

CIT constant initial temperature.

FEA finite element analysis.

FSW friction stir welding.

FVM finite volume method.

HAZ heat affected zone.

LBW laser beam welding.

SoC state of charge.

TIG tungsten inert gas.

TMAZ thermomechanically affected zone.

Chapter 1

Report Structure

The structure of this report is based around three main parts. **Beginning** with introductory information, purpose and what is to be expected of the work. **Middle** part which is the main body of work, including the three methods of evaluation / analysis. Each having introduction, and ending comments. **Ending** with total conclusions and further recommendations.

- **Beginning:** Background, Introduction and Problem description. Chapters 2, 3, 4 and 5.
- **Middle:** Main body of work:
  - Calculations on weld strength. Chapter 6.
  - FEA on weld geometry. Chapter 7.
  - Temperature simulations, welding process Chapter 8
- **Ending:** Conclusions & Recommendations. Chapter 9.

Chapter 2

Background

2.1 Northvolt

Northvolt, a newcomer to the battery manufacturing industry, was founded in 2016 with the goal of building the world's greenest battery to enable the European transition to renewable energy. A high ambition on how to handle their products at their end-of-life, such as using recycled material from old cells to use in the production of new cells. As a company still in early stages of business, 2018 was the year in which northvolts first product was delivered to customer, and in 2019 they produced their first prismatic cell.

The northvolt mission: establish a European supply chain of batteries, beginning with Europe's largest battery cell factory with annual production of 40 GWh. Clean energy, sustainable processes and recycling are all central to their vision. One of the goals is to have a circular system in which old battery packs can be recycled in order to to source and refine the raw materials needed for the production of new batteries. *Northvolt, 2020*

2.2 Prismatic Cell Modules

Battery packs are usually built up by assembling cells in sub-assemblies called modules. The modules themselves can then be arranged and assembled in configurations according to requirements and specifications into a battery pack. This can continue, with a less clear naming scheme, with battery packs connected together to form larger systems. This paper focuses on the joining stage of a *module*, with more precise wording, welding / joining a prismatic cell module.

2.3 Prismatic Battery Cells

A prismatic battery cell is named after its prismatic / rectangular shape and are commonly found in cell-phones or in laptop batteries in smaller sizes. Prismatic cells are usually encased in an aluminium or steel housing, which adds stability and structure. In addition to this structure, additional compression of the cells can be applied to maintain battery health over cycle life. *Barai et al., 2017*

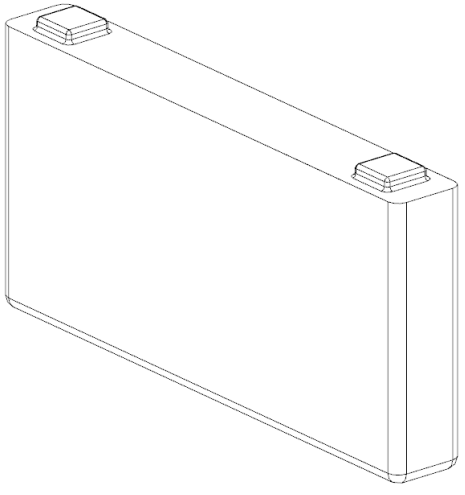

Figure 2.1: Sketch of a prismatic cell

Large size prismatic cells have starting to gain popularity within the automotive industry, mainly due to their high specific energy and high energy density. They have a high capacity and the number of cells required for a battery pack is therefore relatively low. As of their prismatic shape, they are easy to assemble and facilitate elegant packaging solutions. A relatively low number of connections is required because of the low number of required cells. *Berg et al., 2020.* This in relation to something like the more common cylindrical battery cells, which generally are a bit smaller, and the cylindrical shape limiting packaging density / efficiency. A sketch of a large format prismatic cell can be seen in figure 2.1. One of the major drawbacks with large prismatic cells is the relatively low available surface area for cooling.

2.4 Purpose

The purpose of this thesis to evaluate the implementation of tungsten inert gas (TIG), friction stir welding (FSW) or laser beam welding (LBW) to join an aluminium prismatic cell - module frame. The evaluation is based on two main requirements.

- Welding method must be capable of forming a weld that can withstand the swelling forces of the cells.
- The welding method must not heat up the cells to unsafe temperatures.

One of the goals of this thesis is also to establish and create tools for further internal analysis. There is therefore also a focus on performing the analysis and standardising the methods used in order to later validate them. This with the intention to possibly use the same methods and tools in further research and development.

2.4.1 Demarcations

The types of joints that will be investigated will be a TIG weld, a FSW weld and a LBW weld. No other joining methods will be investigated. No other materials, including alloys, will be investigated other than a 6060 T6 aluminium alloy and a 5754 H11 alloy for the welded frame. See section 6.1 In this report, different techniques are used to compare weld strengths. The results should be used for comparison only and not to be used as absolute dimensioning calculations. The three above mentioned welding methods will be investigated with one specified welding geometry each. Initial thought have been given to using alternative fastening methods and materials. However, work has already been put into designing a frame to be extruded out of aluminium, and welding is the preferred fastening method. Any relevant analysis of other fastening methods would need to include changes to design and further investigation of assembly method.

Chapter 3

Welding Aluminium

3.1 General Material Properties

Aluminium is about six times more thermally conductive than compared to steel, and has a specific heat of almost double. However, aluminium has a lower melting point. Aluminium surfaces also rapidly oxidizes when exposed to air, forming an aluminium oxide layer on the surface which can be difficult to remove or melt during welding processes. Welding aluminium with a requirement on low spread of heat can therefore be challenging.

3.2 Heat Affected Zone

The heat affected zone (HAZ) is defined as the parts of the weld / base material which has not only been heated by the welding process, but in which metallurgical changes have occurred. See figure 3.1. For strain hardened metals and alloys, the material in the HAZ can loose strength due to the loss of dislocations. Precipitation hardened alloys, (*also called age hardened*), will loose some of the hardening as a result of the dissolving of precipitates. This is also true for the weld fusion area. *Forsman, 2000.*

As stated by *Pradeep Sensharma, 2010 " it is further clear that the 6061-T6 alloy suffers a larger reduction in ultimate tensile strength than the 5083-H116 al-*

loy. This is a result of the different metallurgy of the two alloys, the 5xxx-series alloys are strain-hardened, so they regain much of their pre-welded strength via cold working when the welds are loaded plastically. However, the 6061-T6 is a precipitation-hardened alloy that does not significantly work-harden when re-loaded, and looses much of its ultimate tensile strength as well as its proof stress when welded"

In *"Eurocode 9: Design of aluminium structures", 2007*, (table 3.2) values for material properties can be found. Including their welded properties, such as their HAZ strength. Also the extent of the HAZ can be found in *"Eurocode 9: Design of aluminium structures", 2007*, (figure 6.6) and is described for the alloys in 6xxx series and 5xxx series as used in this study, for thicknesses below 6 mm as extending 30 mm.

In short, material in the HAZ can suffer loss of the properties gained by tempering.

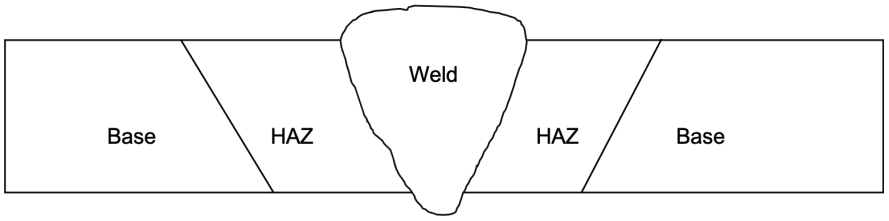

Figure 3.1: Cross sectional view of a butt weld with HAZ labeled

3.3 Hot Cracking

Hot cracking, also known as solidification cracking, occurs when molten metal solidifies during a weld operation. The contraction that occurs leads to high internal tensile stresses from which cracks can form. Alloying elements in aluminium can be used to change its ductility and with that its crack sensitivity. In figure 3.2, the cracking sensitivity of alloyed aluminium can be seen, and shows that the chemistry of the welded aluminium is important to resist cracking. As stated by *P. Kah and Martikainen, 2010*, the aluminium alloys of the 6xxx - series have a high crack-sensitivity since most of the alloys in

that series have a 1.0 % Magnesium Silicide (Mg_2Si) content, which is close to the peak of the crack sensitivity curve, as seen in figure 3.2. A higher crack sensitivity naturally leads to a weaker weld.

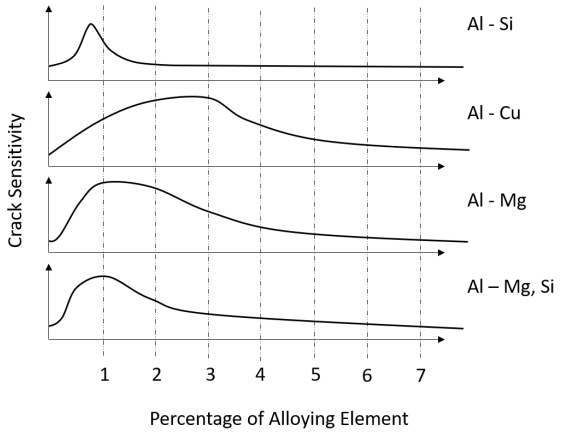

Figure 3.2: Alloying content vs Cracking Sensitivity. 6xxx series in the bottom row, Mg, Si.

In appendix E, two sample pull tests are performed, one where a 6xxx series is welded to itself, and one where 6xxx series is joined with an alloy from the 5xxx series of aluminium, increasing the alloying content and thereby also lowering the crack sensitivity.

3.4 Welding methods

TIG welding

TIG, tungsten inert gas welding, also known as (GTAW), is a welding method in which a non-consumable electrode is used to melt metals by producing a heating arc between the electrode and the work piece. This is performed using a shielding inert gas, and usually with the addition of a filler material that changes the chemical composition of the weld relative to the base material. TIG welding is generally a manual process that requires a high operator skill to produce reliably and is generally hard to automate. TIG welding is a relatively slow process as compared to the other welding methods in this report.

FSW

FSW, friction stir welding, is a solid state process, where the base material is heated by a spinning, non-consumable, tool head that plunges down into the work piece, traverses along the weld axis, thermo-mechanically stirring / mixing the base material together. Therefore, in addition to a HAZ, as described in section 3.2, a FSW weld also has a thermomechanically affected zone (TMAZ) between the weld nugget and the HAZ. See figure 3.3. As the heat generation of FSW mainly comes from friction and the plastic work done to the base material, the welding temperature stabilizes near the solidus temperature of the base material *Colligan, 2010*.

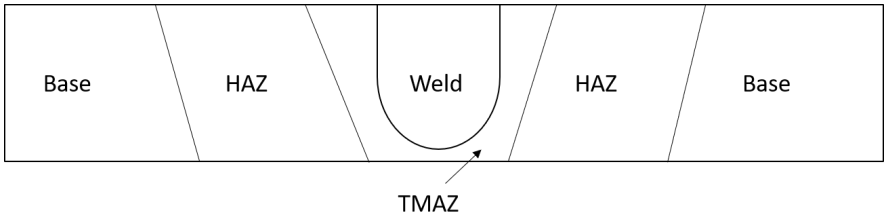

Figure 3.3: Cross sectional view of an FSW joint, with labeled zones

FSW is a quite fast, reliable and automated process. However, as a result of the high forces produced by the plunging and transverse movement of the

spinning tool head, high clamping forces are required to fixate the parts to be joined.

LBW

LBW, laser beam welding, is a welding method where materials can be joined by heating with a high powered, focused laser. The laser is absorbed by the surface layer and a vapour capillary forms a keyhole in the base material, heating the surrounding material. Laser welding is a fast and automated process.

According to *Forsman, 2000*, LBW welds are prone to hot cracking such as described in section 3.3 and can have pores formed by dynamic keyhole motion. Both of which can be minimized by slowing the process speed and lowering the power intensity at the same time. Pores in a LBW can also form a result of precipitated hydrogen from unclean surfaces.

Chapter 4

Problem

4.1 Cell Swelling

Swelling of cells is a complicated process with many different variables which is researched extensively. This section is meant to illustrate the problems with cell swelling, since researching it is a masters thesis on its own. As shown by *Oh and Epureanu, 2016*, prismatic lithium - ion cells swell due to a number of factors. One type of swelling occurs as a result of the cell temperature, charge/discharge rate as well as the state of charge (SoC), *Oh et al., 2014*. Another type of swelling arises while charge cycling the cells. This swelling is a result of irreversible chemical reactions according to *Jae Hyun LeeH, 2003*. As a swell scale reference, in their report, *Oh et al., 2014* measured an cell expansion of about 1.5 % due to swelling related to the cells SoC. The swelling is most noticeable on the middle of the large faces on the cells.

The forces involved in cell swelling is rather complex and depend greatly on the boundary conditions. According to *(Ki-Yong Oh, 2017) "The initial displacement is important to accurately predict reaction forces because the reaction forces depend nonlinearly on the swelling. The larger the initial displacement is, the more curved is the parabolic shape of the relation between force and swelling"*.

4.2 Description

This thesis investigates and compares three weld-joining methods for a prismatic cell module. The weld that is being investigated is the weld on the frame, that encases the row of cells, *the cell stack*. As starting point for this thesis, the frame is constructed out of 6060 T6 aluminium alloy. See figure 4.1.

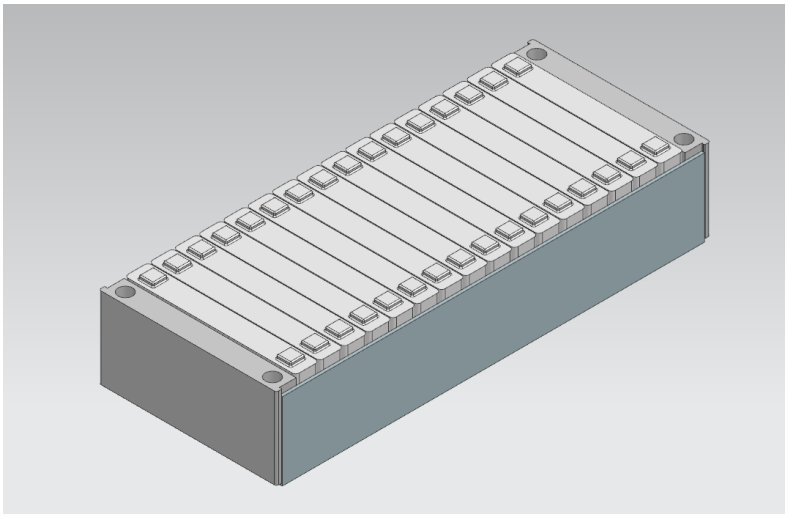

Figure 4.1: Simplified version of the module with a stack of cells.

Assembly of a module

With the cells in place (in a low SoC), the frame, consisting of two sidewalls and two endplates, is pressed against the cells either within a specified pressure range or at a specified distance, and is then joined, resulting in a pre-load on the cell stack. Not only will the frame of the module have to withstand the force of the pre-load, but since the cells are in a low-charge state when the frame is joined, and since cells swell due to a number of factors including SoC, as explained in section 2.3 the frame will have to withstand an even higher load-case when charged and over time. The load case for the frame is provided by *northvolt* as a 30 kN load. See figure 4.2. The cell swelling is not expected

to result in any load case in the sideplate-sideplate direction of the module, since the concern of swelling is mostly regarding the large faces of the cells, which also happens to be the direction in which the cells are stacked.

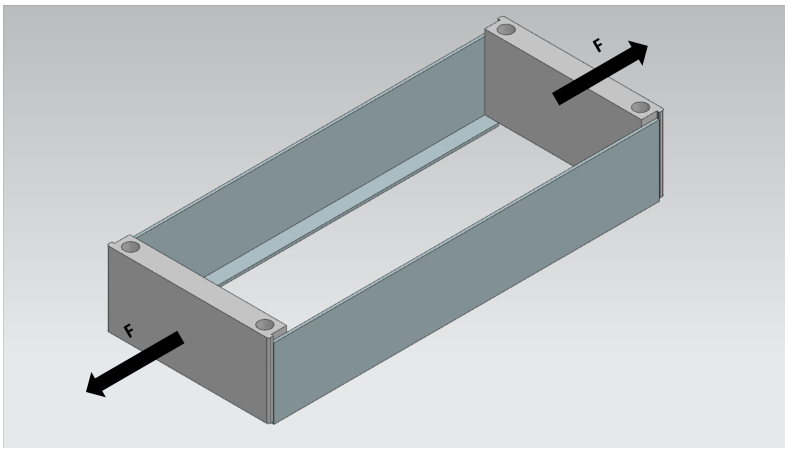

Figure 4.2: Simplified version of the module. Force is approximated as pressure on the surface.

Since this module is welded with live cells in place, it is very important that the temperature on the cell side does not reach temperatures that would be harmful to the cells. In operation, the temperature of these cells should not reach above 60 deg C, but in this thesis, a temporary maximum temperature of under 80 deg C will be used as design requirement as this should be a safe passive temperature during a short period of time, at the relatively low SoC the cells are at during assembly.

4.2.1 Requirements

The requirements have now been expressed and are as follows.

- Withstand load case of 30 kN.
- Temperature on cell side staying below 80 deg C

4.3 Load Case simplification

The calculations were simplified by assuming that the model and load-case is symmetric in all four quadrants as shown in figure 4.3.

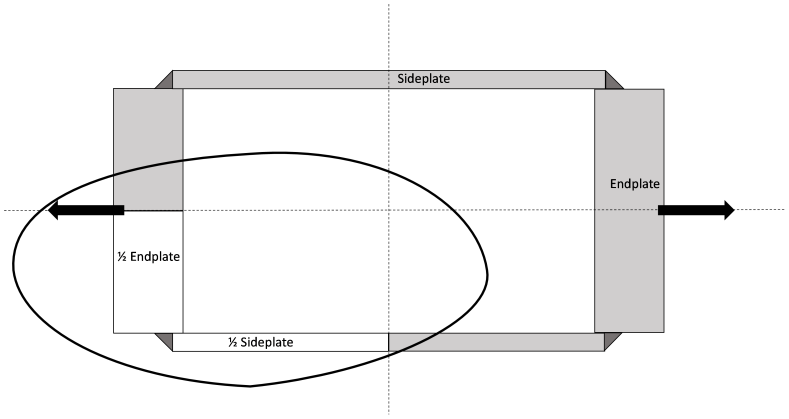

Figure 4.3: Top view of the full body TIG weld and the load-case. Calculations are simplified by only calculating circled part (quadrant 3) and assuming symmetry.

Since the model and load case is symmetric in all four quadrants, the load case is simplified to a 2D load case as shown in figure 4.4, assuming a stiff endplate that does not deform. With the assumption that the load is distributed symmetrically, the load case is halved to 15 kN for this quarter model.

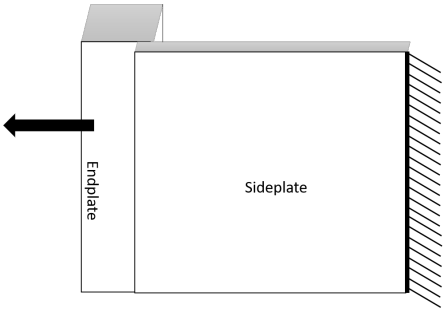

Figure 4.4: Load case simplified from a 3D load-case to a 2D load case.

Chapter 5

Process

Literature Study

Firstly a literature study is performed to get an understanding of the characteristics of each welding technique.

Initial Calculations & FEA

Second, a number of initial calculations were performed as in appendix C. This worked as a first screening of the welding methods and to develop an understanding of the possibilities of the methods. These calculations were accompanied by initial FEA on all welds and their respective suggested geometries. See appendix D.

Specification of Weld Geometry

Third, a weld geometry is specified for each welding method with approximated equal weld leg lengths.

After the initial calculations and FEA were performed, the geometry specification for the LBW was changed from an overlap weld to a fillet weld. As a result of new information from northvolt. See figure 5.1.

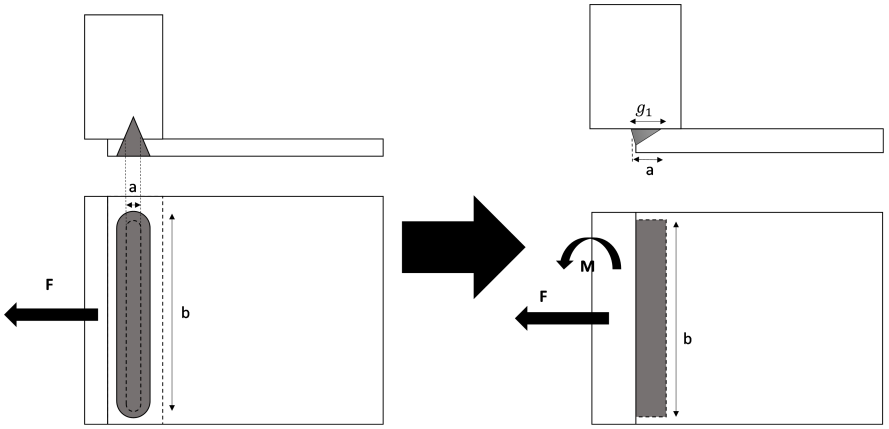

Figure 5.1: Geometry change for the LBW from initial calculations and FEA.

Calculations

With this specified geometry, weld strength calculations are performed in accordance with the specified load case to an approximated Eurocode 9 standard. See chapter 6.

FEA

The calculations are then again followed by FEA evaluation and comparison to the calculations. See chapter 7

Simplified Thermal Development

Lastly a simplified thermal development simulation model is set up for each process and compared to very limited trial data as to evaluate the possibility of passing the temperature requirement stated in section 4.2.1. See chapter 8

Chapter 6

Eurocode Calculations

6.1 Materials

The aluminium frame is constructed out of 6060 T6 aluminium. This will be true for all performed calculations, except for the calculations on LBW in section 6.5, where the choice of sideplate material is 5754 H11 aluminium. This is because the otherwise very high crack sensitivity that a LBW consisting of two pieces of 6060 T6 aluminium would produce without any filler material, as explained in section 3.3. See also appendix E, where a sample of 6082-6082 LBW fillet weld was tested and compared against a 6082-5754 LBW fillet weld. LBW of two pieces of 6060 T6 aluminium with a filler material is shortly explored in section 9.3 *LBW with filler material*.

6.2 Approximations for FSW and LBW

Eurocode calculations for the TIG weld can be performed. But since it does not cover FSW or LBW, a few approximations / assumptions are made. It is important to note that these are calculations for comparison, and not dimensioning calculations.

6.3 Eurocode 9 TIG calculation

A body diagram of the TIG weld can be seen in figure 6.1 and describes how the a-dimension is conservatively approximated.

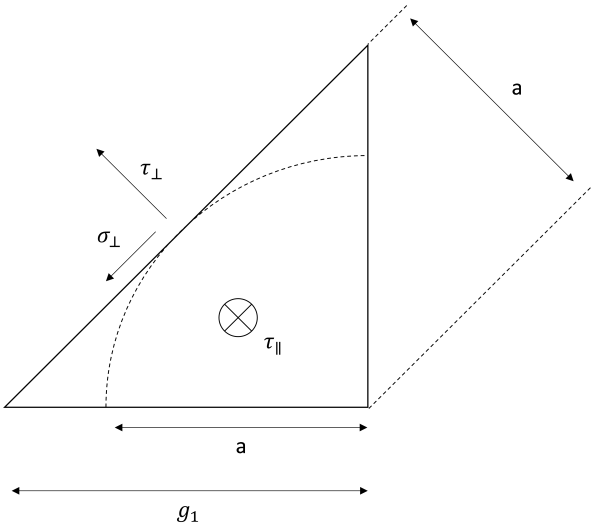

Figure 6.1: Free body diagram of a TIG weld

TIG load case

The weld geometry is described in figure 6.2.

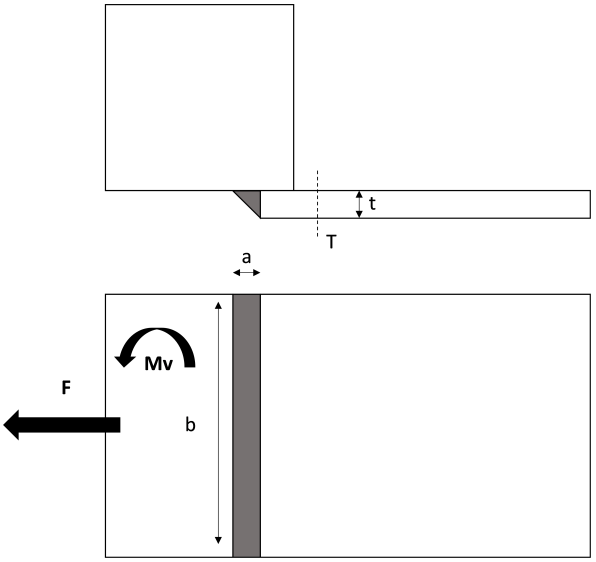

Figure 6.2: TIG weld geometry

The load case is described by a normal force and a moment applied to the endplate (left larger plate).

The moment is derived from the actual load case as described in figure 6.3, as $M = F \cdot l_m$.

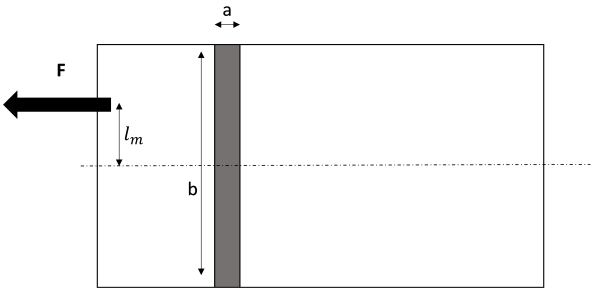

Figure 6.3: Load case before simplification

Eurocode 9 requirements

When dimensioning a fillet weld according to Eurocode 9, the following requirements in equations 6.1 and 6.2 need to be fulfilled.

$$\sigma_{VM} = \sqrt{\sigma_{\perp,Ed}^2 + 3 \cdot (\tau_{\perp,Ed}^2 + \tau_{\parallel,Ed}^2)} \leq \frac{f_w}{\gamma_{Mw}} \tag{6.1}$$

Where f_w is the characteristic strength of weld metal and γ_{Mw} is the partial safety factor for welded joints. σ_{VM} is the Von-Mises equivalent stress. $\sigma_\perp$, $\tau_\perp$ and $\tau_\parallel$ can be seen in figure 6.1.

$$\begin{cases} weldtoe : \sigma_{haz,Ed} \leq \frac{f_{u,haz,TIG}}{\gamma Mw} \\ fusionboundary : \sigma_{haz,Ed} \leq \frac{g_1}{t} \frac{f_{u,haz,TIG}}{\gamma Mw} \end{cases} \tag{6.2}$$

Where $\sigma_{haz,Ed}$ is the design normal stress perpendicular to the weld axis at the toe of the weld *(full cross section of the plate)* and at the fusion boundary. $f_{u,haz,TIG}$ is the characteristic strength of the HAZ for TIG welds, and is derived from $f_{u,haz} \cdot 0.8$ as stated in table 3.2b in Eurocode 9. g_1 is the weld leg length as displayed in figure 6.4 and t is the thickness of the plate.

Calculations

In this case, the worst case for the stress in the weld is easily identifiable as the most distant point of the weld where the stresses caused by the force and by the moment are added.

The uniformal stress as a result of the force F can be calculated as in equation 6.3.

$$\sigma_F = \frac{F}{a \cdot b} \tag{6.3}$$

At the top of the weld, $\sigma_{M,max}$ as a result of the moment can be described as in equation 6.4.

$$\sigma_{M,max} = \frac{M \cdot r_y}{I} \tag{6.4}$$

Where $r_y = b/2$ is the distance from the centroid of the weld body to the furthest point of the weld. And I is the moment of inertia of the weld and is expressed as in equation 6.5.

$$I = \frac{1}{12} \cdot a \cdot b^3 \tag{6.5}$$

The total maximum stress can then be expressed as in equation

$$\sigma_{max} = \sigma_F + \sigma_{M,max} \tag{6.6}$$

The weld stresses are shown in figure 6.4.

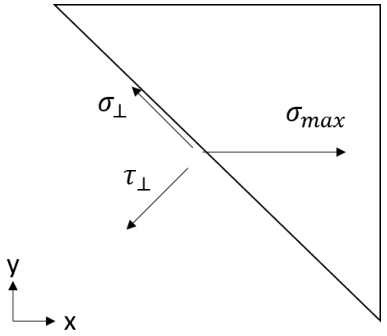

Figure 6.4: Free body diagram of a TIG weld with σ_{max} applied

As can be seen in figure 6.4, equilibrium equations can be set up as in equation 6.7.

$$\begin{cases} x : \sigma_{max} - \frac{\sigma_\perp}{\sqrt{2}} - \frac{\tau_\perp}{\sqrt{2}} = 0 \\ y : \sigma_\perp - \tau_\perp = 0 \end{cases} \tag{6.7}$$

The equilibrium in the y dimension shows that $\sigma_\perp = \tau_\perp$ and therefore the equilibrium for the x direction can be expressed as in equation 6.8.

$$\sigma_\perp = \tau_\perp = \frac{\sigma_{max}}{\sqrt{2}} \tag{6.8}$$

Since there is no lateral loading $\tau_\parallel = 0$, the requirement in equation 6.1 can now be checked.

For the requirement in equation 6.2, $\sigma_{haz,Ed}$ needs to be calculated for the full cross section at the toe of the weld and for the fusion boundary. The stress $\sigma_{haz,Ed}$ at the fusion boundary is calculated analogously to the stress σ_{max} but with all dimensions of a changed to the leg length g_1. With the stresses at the fusion boundary being higher than the ones at the toe of the weld, checking for the fusion boundary is sufficient.

The values as derived from Eurocode 9 are presented in table 6.1.

Table 6.1: Variable values as retrieved from Eurocode 9, Single fillet weld using material 6060 and filler 5356

Variable	*Value*	*Unit*
$f_{u,haz}$	100	MPa
$f_{u,haz,TIG}$	80	MPa
f_w	160	MPa
γ_{Mw}	1.25	Dimensionless

Problem defined values and results are presented in table 6.2.

Table 6.2: Input values and results for the TIG weld

Variable	*Value*	*Unit*
Input		
a	2.83	mm
b	100	mm
F	15	kN
g_1	4	mm
l_m	4.75	mm
M	71.25	Nm
t	4	mm
Results		
σ_{VM}	96.375	MPa
$\sigma_{haz,Ed}$	48.188	MPa

The requirements can now be checked from equation 6.1 and 6.2 below in equation 6.9 and 6.10.

$$\sigma_{VM} = 96.375MPa \leq \frac{f_w}{\gamma_{Mw}} = 128MPa \quad OK! \tag{6.9}$$

$$\sigma_{haz,Ed} = 48.188MPa \leq \frac{g_1}{t}\frac{f_{u,haz,TIG}}{\gamma Mw} = 64MPa \quad OK! \tag{6.10}$$

6.4 Approximated Eurocode 9 FSW calculation

The FSW uses similar parameters as the TIG calculations. However, as no filler material is used, and as a result of the low heat generation, the f_w and $f_{u,haz}$ are revised.

Revised f_w and $f_{u,haz}$ for FSW

In Eurocode 9, $f_{u,haz}$ is calculated by using the strength of the base material $f_u = 170MPa$ and multiplying it with the HAZ factor $\rho_{u,haz=0.59}$ for TIG welding and then further reduced by a factor of 0.8. For the FSW, $f_{u,haz}$ will be calculated with a value of $\rho_{u,haz=0.8}$ and therefore we will have that $f_{u,haz,FSW} = 136MPa$. The weld bead characteristic strength f_w is retrieved from table 8.8 in Eurocode 9 by filler material and base material, but will in this case be regarded as equal to $f_{u,haz,FSW}$.

The values as derived or revised from Eurocode 9 for the FSW calculations are presented in table 6.3.

Table 6.3: Variable values as retrieved from Eurocode 9 for FSW

Variable	*Value*	*Unit*
f_u	170	MPa
$f_{u,haz,FSW}$	136	MPa
γ_{Mw}	1.25	Dimensionless
$\rho_{u,haz}$	0.8	Dimensionless

Loadcase & Description

The FSW is an overlap weld. The geometry can be seen in figure 6.5.

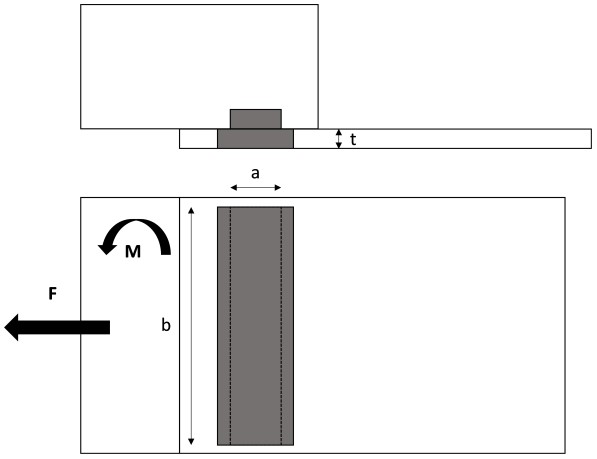

Figure 6.5: FSW weld geometry

The load case is described by a normal force and a moment applied to the endplate (left larger plate) with the moment derived analogously as in section 6.3.

A body diagram of the FSW weld can be seen in figure 6.6.

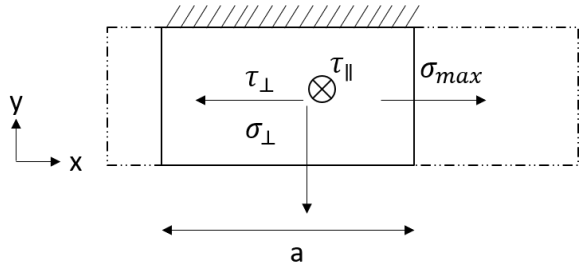

Figure 6.6: Free body diagram of FSW

Eurocode 9 requirements

The same requirements as stated for the TIG weld in section 6.3 will be used and described as in equation 6.11 and 6.12. But with changed values in ac-

cordance with section 6.4, *Revised f_w and $f_{u,haz}$ for FSW.*

$$\sigma_{VM} = \sqrt{\sigma_{\perp Ed}^2 + 3 \cdot (\tau_{\perp Ed}^2 + \tau_{\parallel Ed}^2)} \leq \frac{f_{u,haz,FSW}}{\gamma_{Mw}} \tag{6.11}$$

$$\begin{cases} weldtoe : \sigma_{haz,Ed} \leq \frac{f_{u,haz}}{\gamma_{Mw}} \\ fusionboundary : \sigma_{haz,Ed} \leq \frac{g_1}{t} \frac{f_{u,haz,FSW}}{\gamma_{Mw}} \end{cases} \tag{6.12}$$

Calculations

The worst case stresses occur analogously the TIG worst case at the top of the weld and is calculated analogously.

$$\sigma_{max} = \sigma_F + \sigma_{M,max} \tag{6.13}$$

The free body diagram of the FSW in cross section with σ_{max} applied can be seen in figure 6.6. From this figure, it is clear that the stress is reacted purely in shear stress perpendicular to the weld axis, which the equilibrium equation, equation 6.14 shows.

$$\sigma_{max} - \tau_{\perp} = 0 \tag{6.14}$$

σ_{VM} can now easily be calculated as in equation 6.15, simplified from equation 6.11 since $\sigma_{\perp} = 0$ and $\tau_{\parallel} = 0$.

$$\sigma_{VM} = \sqrt{3} \cdot \tau_{\perp} \tag{6.15}$$

Problem defined values and results are presented in table 6.4.

Table 6.4: Input values and results for the TIG weld

Variable	*Value*	*Unit*
Input		
a	4	mm
b	90	mm
F	15	kN
g_1	4	mm
l_m	4.75	mm
M	71.25	Nm
t	4	mm
Results		
σ_{VM}	95.022	MPa
$\sigma_{haz,Ed}$	54.86	MPa

The requirements can now be checked from equation 6.11 and 6.12 below in equation 6.16 and 6.17.

$$\sigma_{VM} = 95.022MPa \leq \frac{f_w}{\gamma_{Mw}} = 108.8MPa \quad OK! \tag{6.16}$$

$$\sigma_{haz,Ed} = 54.86MPa \leq \frac{g_1}{t}\frac{f_{u,haz}}{\gamma Mw} = 108.8MPa \quad OK! \tag{6.17}$$

6.5 Approximated Eurocode 9 LBW calculation

After the initial LBW calculations performed in appendix C.1.3, the specified method of laser welding is changed slightly into a fillet lap weld instead of an overlap weld. Also, in contrast to both the TIG and the FSW, a new material choice *AI 5754 H11* is considered for the side plate displayed in figure 6.7.

Loadcase & Description

The new LBW is a fillet type weld. The geometry can be seen in figure 6.7.

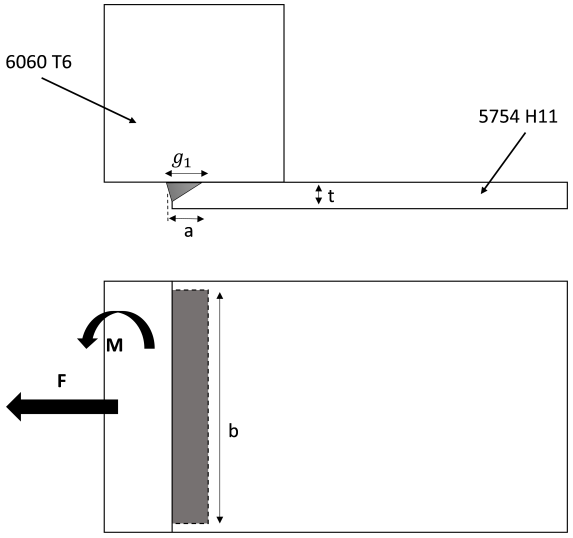

Figure 6.7: LBW weld geometry

The load case is described by a normal force and a moment applied to the endplate (left larger plate) with the moment derived analogously section 6.3.

A body diagram of the LBW weld can be seen in figure 6.8 and describes how the a-dimension is conservatively approximated.

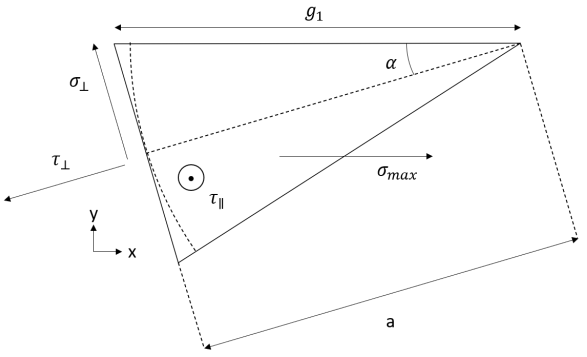

Figure 6.8: Free body diagram of a LBW weld

Revised f_w and $f_{u,haz}$ for LBW

Analogously section 6.4, the values of f_w and $f_{u,haz}$ need to be revised for LBW in order to be comparable to the TIG weld. As the $f_{u,haz} = 100$ MPa for the 6060 alloy is significantly lower than the $f_{u,haz} = 180$ MPa for the 5754 alloy, the conservative assumption is made that $f_W = f_{u,haz,6060}$.

The values as derived or revised from Eurocode 9 for the FSW calculations are presented in table 6.5.

Table 6.5: Variable values as retrieved from Eurocode 9 for LBW

Variable	*Value*	*Unit*
$f_{u,5754}$	180	MPa
$f_{u,6060}$	170	MPa
$f_{u,haz,6060}$	100	MPa
f_w	100	MPa
γ_{Mw}	1.25	Dimensionless

Eurocode 9 requirements

The same requirements as stated for the TIG weld in section 6.3 will be used and described as in equation 6.18 and 6.19. But with changed values in ac-

cordance with section 6.5, *Revised f_w and $f_{u,haz}$ for LBW.*

$$\sigma_{VM} = \sqrt{\sigma_{\perp Ed}^2 + 3 \cdot (\tau_{\perp Ed}^2 + \tau_{\parallel Ed}^2)} \leq \frac{f_w}{\gamma_{Mw}} \tag{6.18}$$

$$\begin{cases} weldtoe : \sigma_{haz,Ed} \leq \frac{f_{u,haz}}{\gamma Mw} \\ fusionboundary : \sigma_{haz,Ed} \leq \frac{g_1}{t} \frac{f_{u,haz,5754}}{\gamma Mw} \end{cases} \tag{6.19}$$

Calculations

The worst case stresses occur analogously the TIG worst case at the top of the weld and is calculated analogously.

$$\sigma_{max} = \sigma_F + \sigma_{M,max} \tag{6.20}$$

Equilibrium equations can be derived from figure 6.8 as in equation 6.21.

$$\begin{cases} x : \sigma_{max} - \sigma_\perp \cdot \sin\alpha - \tau_\perp \cdot \cos\alpha = 0 \\ y : \sigma_\perp \cdot \cos\alpha - \tau_\perp \cdot \sin\alpha = 0 \end{cases} \tag{6.21}$$

From the y axis $\sigma_\perp$ can be solved for as in equation 6.22

$$\sigma_\perp = \tau_\perp \cdot \tan\alpha \tag{6.22}$$

Which can be used to solve for $\tau_\perp$ with the equilibrium in the x axis as in equation 6.23.

$$\sigma_{max} - \tau_\perp \cdot \tan\alpha \cdot \sin\alpha - \tau_\perp \cdot \cos\alpha = 0 \tag{6.23}$$

In which $\tau_\perp$ can be solved for and simplified as in equation 6.24.

$$\tau_\perp = \sigma_{max} \cdot \cos\alpha \tag{6.24}$$

Which gives from equation 6.22 the following in equation 6.25.

$$\sigma_{\perp} = \sigma_{max} \cdot \sin \alpha \tag{6.25}$$

Problem defined values and results are presented in table 6.6.

Table 6.6: Input values and results for the LBW weld

Variable	*Value*	*Unit*
Input		
α	15	deg
a	3.8638	mm
b	100	mm
F	15	kN
g_1	4	mm
l_m	4.75	mm
M	71.25	Nm
t	4	mm
Results		
σ_{VM}	84.14	MPa
$\sigma_{haz,Ed}$	49.35	MPa

The requirements in equation 6.18 and 6.18 can now be checked as in equation 6.26 and 6.27.

$$\sigma_{VM} = 84.14MPa \leq \frac{f_w}{\gamma_{Mw}} = 80MPa \quad FAILED! \tag{6.26}$$

$$\sigma_{haz,Ed} = 49.35MPa \leq \frac{g_1}{t}\frac{f_{u,haz}}{\gamma Mw} = 78.1MPa \quad OK! \tag{6.27}$$

6.6 Calculation discussion

As a result of the revised values and calculation methods for the FSW and LBW the results should not be used as dimensioning calculations without further testing and validation. The TIG weld shows a good margin for both strength requirements, and should be a viable candidate strength wise. Most interesting however is the results from the LBW weld, which with the initial values of $f_w = 100$ MPa is the only weld to fail the first requirement. This with the assumption that the strength of the weld bead is the HAZ-strength of the end plates weaker alloy. However, it should be a conservative assumption, and since the weld bead should be of a mix of the 6060 and the 5754 alloy, it is possible that the weld bead strength is higher than assumed. With a new assumption that the strength of the weld bead is the average $f_{u,haz}$ strength of the 6060 and 5754, the weld bead strength would be $f_w = 130$ MPa, which would result in a weld strength usage of around 64%, where as the TIG weld strength usage is at about 75% and the FSW weld strength usage at around 88%. This assumption should be somewhat reasonable, since the TIG weld has an increased yield strength with the filler material used, since it further alloys the aluminium and lowers its crack-sensitivity. However, this needs to be validated for the case of the LBW with a 5754 sideplate by further research and / or testing. All of the weld suggestions should therefore be further investigated.

Chapter 7

Finite Element Analysis

7.1 Method

There are many ways of analyzing stresses with FEA. In this paper, a solid element mesh is used. A hot spot method as described by *Lee et al., 2010* is widely used for TIG geometries, but in order to get results that are more easily compared between TIG, FSW and LBW, a number of stresses are investigated and compared. Figure 7.1 shows cross-sections of the three weld types and the positions of in which the equivalent Von-Mises stresses are extracted.

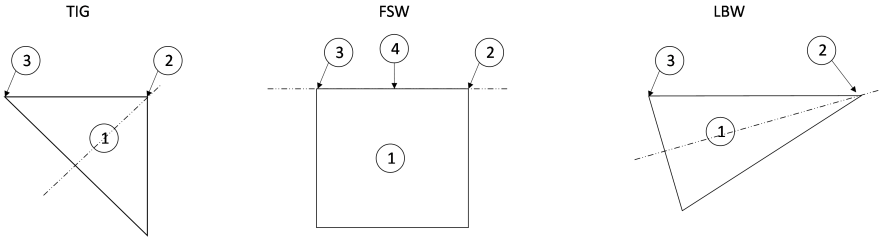

Figure 7.1: Locations of analyzed stresses. 1: Middle of weld, 2: Root, 3: Toe, 4: Extra point for FSW shear-plane. Dashed lines indicate shear-planes.

As point 1 is placed in the middle of the weld body for all cross sections as

shown in figure 7.1, it is also placed in the middle of the shear-stress plane, i.e. the expected failure plane for the TIG and LBW. Point 4 is therefore added to the FSW, in order to get measurements from the middle of the shear plane, the expected failure plane.

From these points, stresses are extracted along the full length of the weld, such as displayed for the TIG weld in figure 7.2.

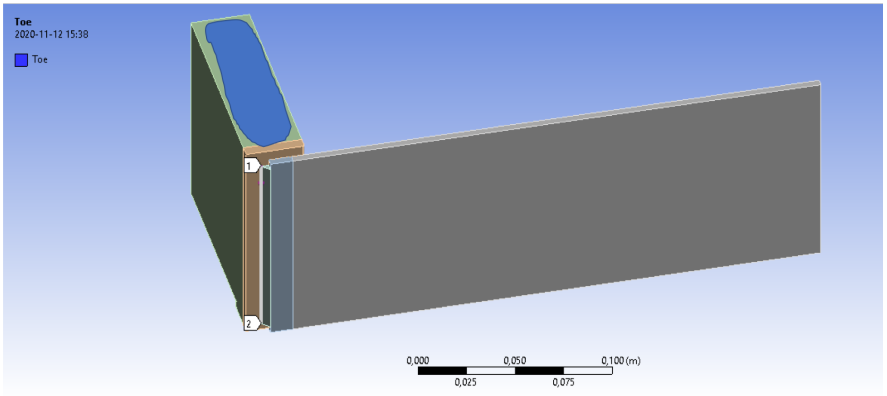

Figure 7.2: Defined axis at the toe of a TIG weld for stress extraction. Axis defined from point 1 to point 2.

7.2 FEA Boundary Conditions

The FEA models are set up with similar approximations and simplifications as in section 4.3. The endplate and sideplate are split in half, assuming symmetry in the quadrants in figure 4.3, and the boundary conditions are set to approximate the boundary conditions as shown in figure 4.4.

The endplate is constrained by frictionless gliding in its split plane, and the sideplate is fixated in its split plane. The force is applied on a specified surface. See figure 7.3.

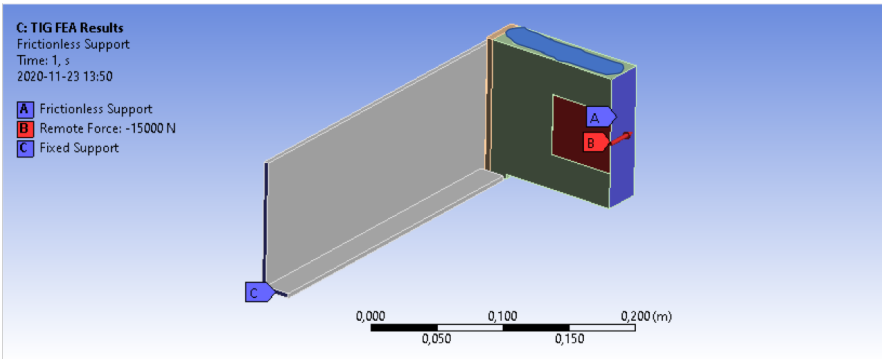

Figure 7.3: Boundary conditions for the FEA models. A: Frictionless gliding in plane. B: Force applied on surface 15 kN at point. C: Fixed constraint.

The endplate and sideplate are both fixed to the weld body with a bonded constraint. Constraint between sideplate and endplate is set as frictionless.

7.3 Mesh size and singularities

When using FEA software to analyze stresses, unrealistically high stresses can occur in sharp corners, mathematical singularity errors. These stresses / errors have a tendency to grow with finer mesh sizes and is one of the difficulties in evaluating welds with the use of FEA software. in figure 7.4 - 7.6 total values of stresses can be seen to increase with a finer mesh for the root of the weld

which is a sharp corner, while the stresses in the middle of the weld body stay relatively consistent with varying mesh size.

First, the *mid* and the *root* stresses are investigated for all three welds with varying mesh size. See figures 7.4 - 7.6. Additionally, the *shear plane* stresses are investigated for the FSW.

7.3.1 Mesh Size and Singularities: Results

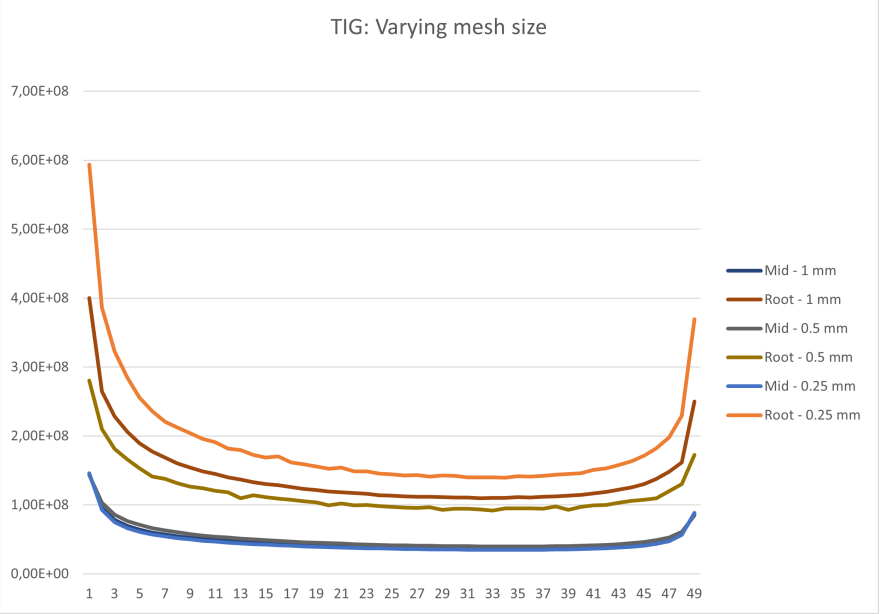

Figure 7.4: Total stresses at root and in mid of weld for TIG with varying mesh sizes. Stress in Pa on Y-axis and sample number on X-axis, with sample 1 being at the top of the weld and sample 49 at the bottom.

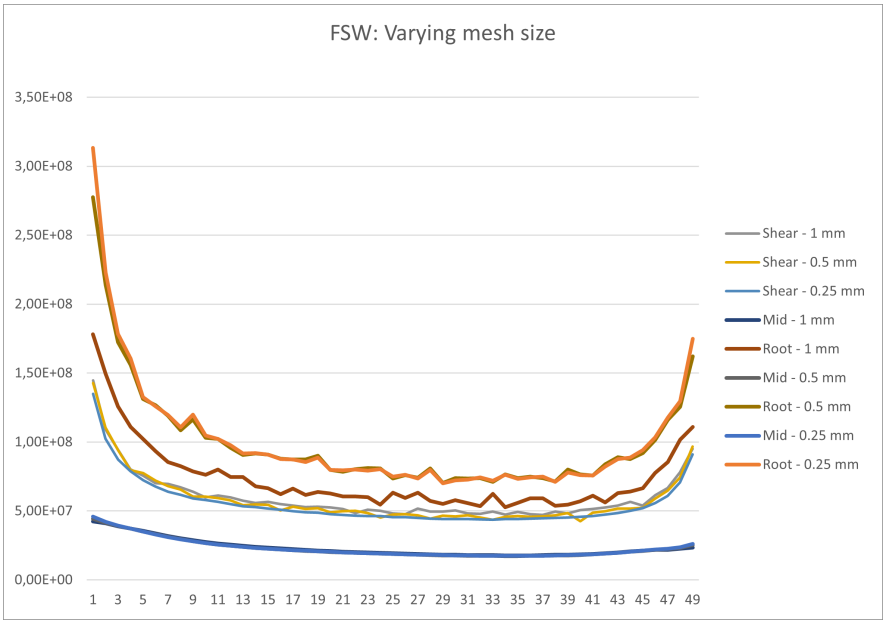

Figure 7.5: Total stresses at root, mid and shear plane of weld for FSW with varying mesh sizes. Stress in Pa on Y-axis and sample number on X-axis, with sample 1 being at the top of the weld and sample 49 at the bottom.

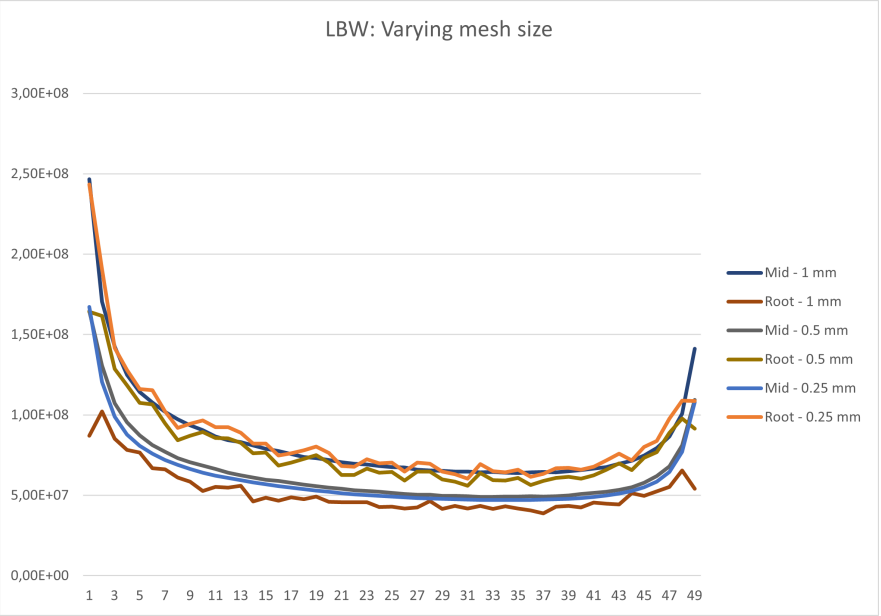

Figure 7.6: Total stresses at root and in mid of weld for LBW with varying mesh sizes. Stress in Pa on Y-axis and sample number on X-axis, with sample 1 being at the top of the weld and sample 49 at the bottom.

It is observed that the stresses seem to have stabilized/converged for the middle of the weld bodies/shearing plane at a mesh element size of about 0.25 mm.

7.4 Non Linear Stresses

In figures 7.4 - 7.6 above, the stresses are extracted as the total stresses, which is a combination of *membrane*, *bending* and *non-linear* stresses. Where the *non-linear* stresses are geometry dependent and notch stresses. See figure 7.7 and 7.8.

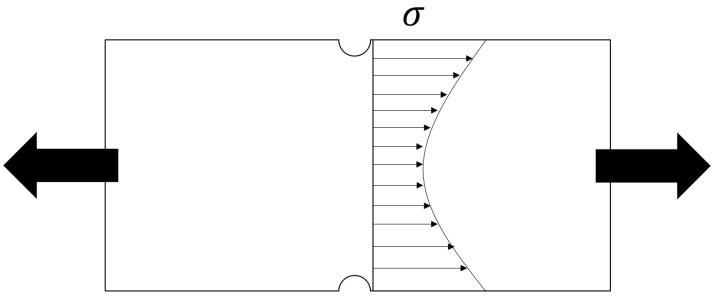

Figure 7.7: Non linear notch stress in a test piece

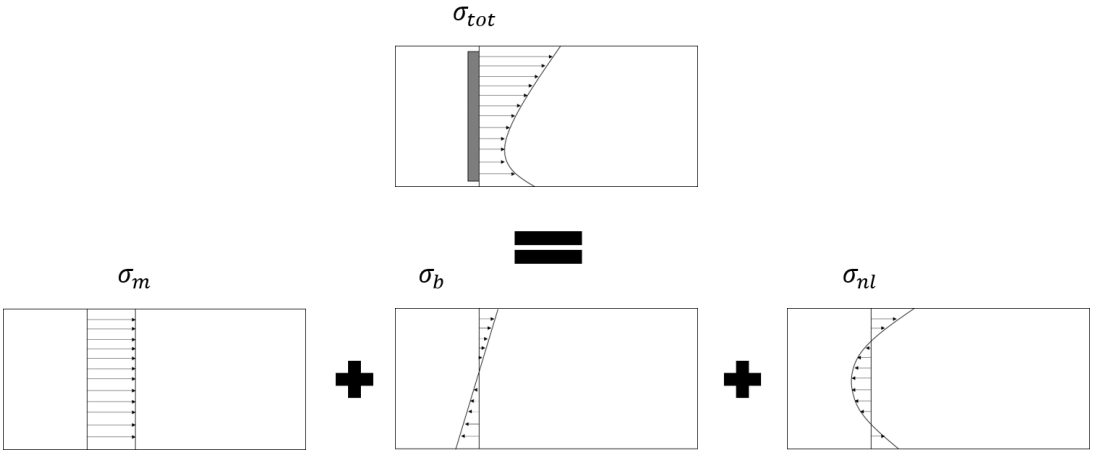

Figure 7.8: Total stress as a combination of membrane stress σ_m, bending stress σ_b and non-linear notch stress σ_{nl}

In the calculations performed in section 6, *Eurocode Calculations*, the non-

linear stresses σ_{nl} are not expressed, and only a membrane + bending combination is used. See figure 7.9.

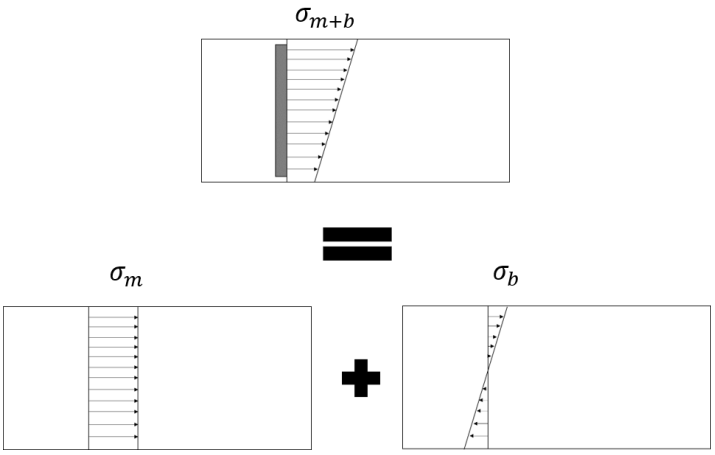

Figure 7.9: Membrane and bending stress combination σ_{m+b}, membrane stress σ_m and bending stress σ_b.

To facilitate the comparison between FEA and the calculations performed in chapter 6, the membrane+bending stress combination should be used as well as the total stresses.

7.5 FEA Results

7.5.1 Stresses

For figures 7.12, 7.15 and 7.18, Stress limits are inserted as calculated in section 6. For the LBW weld, (figure 7.18), the additionally discussed higher stress limit is added as *Stress limit (2)*.

TIG

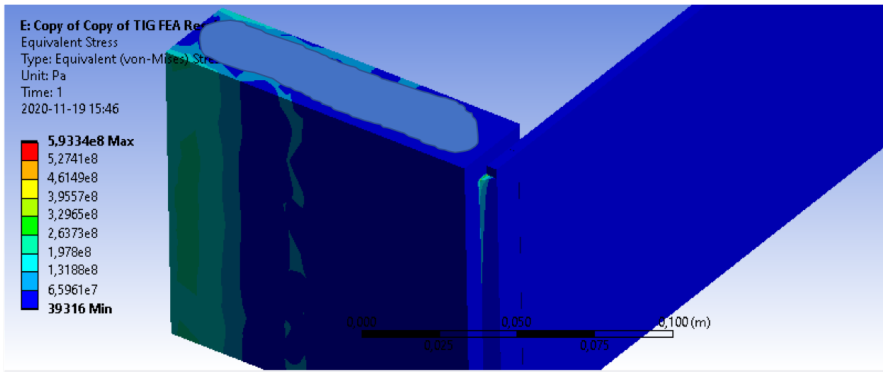

Figure 7.10: View of the TIG FEA model

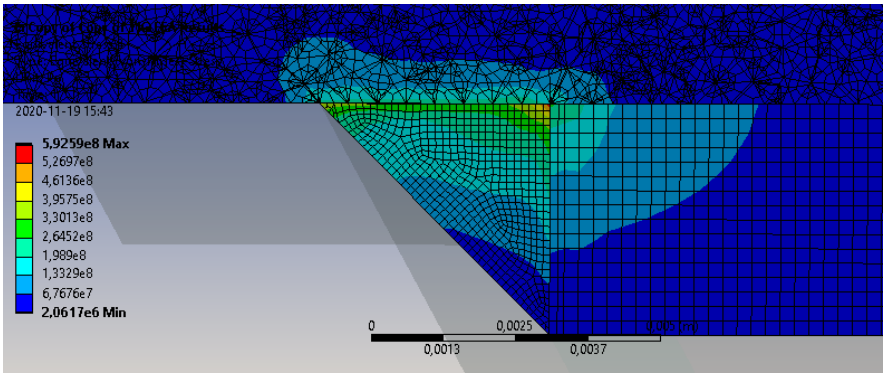

Figure 7.11: Cross section view at the top of the TIG weld bead. Equivalent stress (Von-Mises)

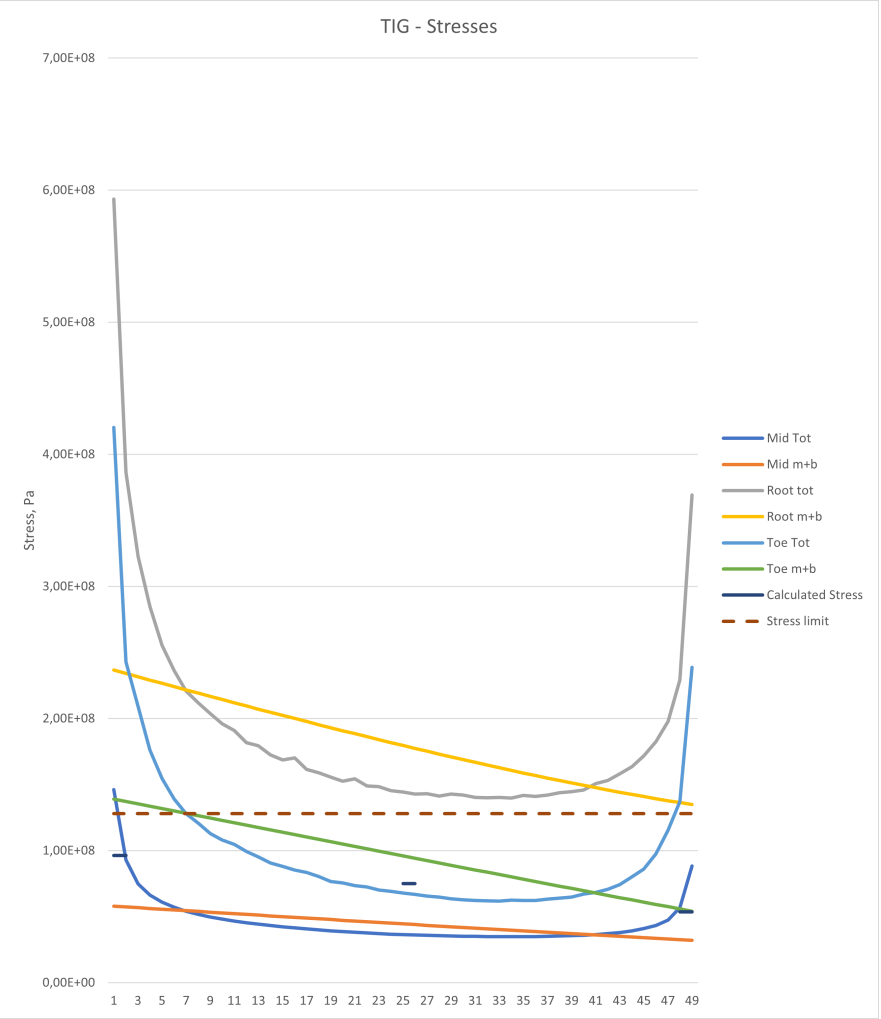

Figure 7.12: Extracted stresses for the TIG weld with element mesh size of 0.25 mm, calculated stresses shown with three dashes for top, mid and bottom of the weld. Stress on the Y-axis in Pa and sample number on the X-axis.

FSW

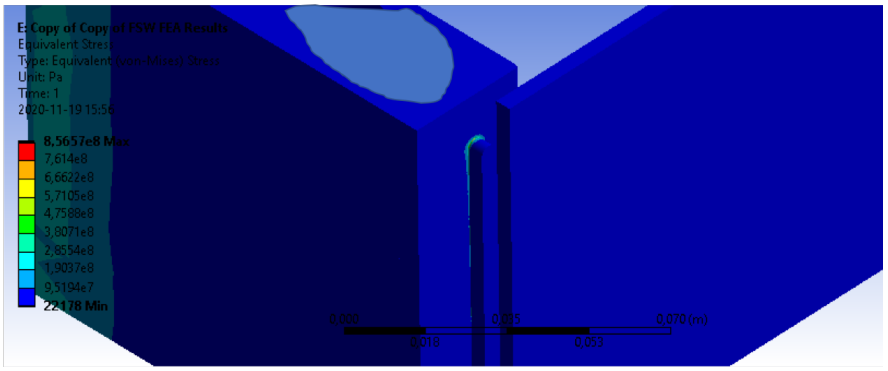

Figure 7.13: View of the FSW FEA model

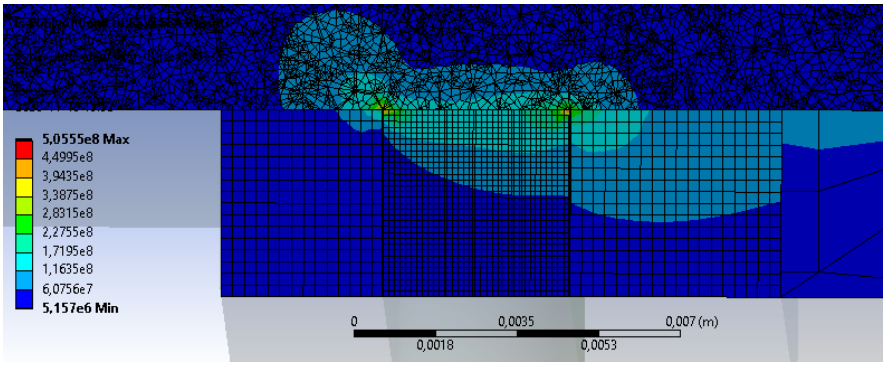

Figure 7.14: Cross section view at the top of the FSW weld bead. Equivalent stress (Von-Mises)

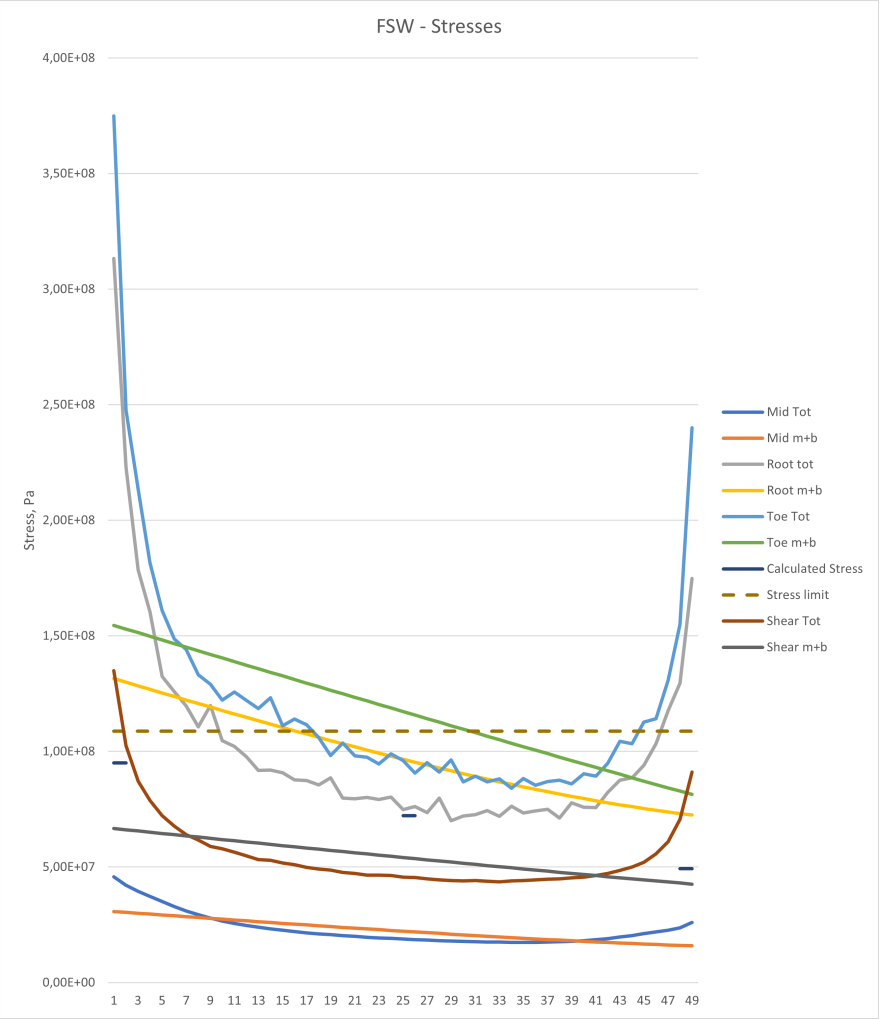

Figure 7.15: Extracted stresses for the FSW weld with element mesh size of 0.25 mm, calculated stresses shown with three dashes for top, mid and bottom of the weld. Stress on the Y-axis in Pa and sample number on the X-axis.

LBW

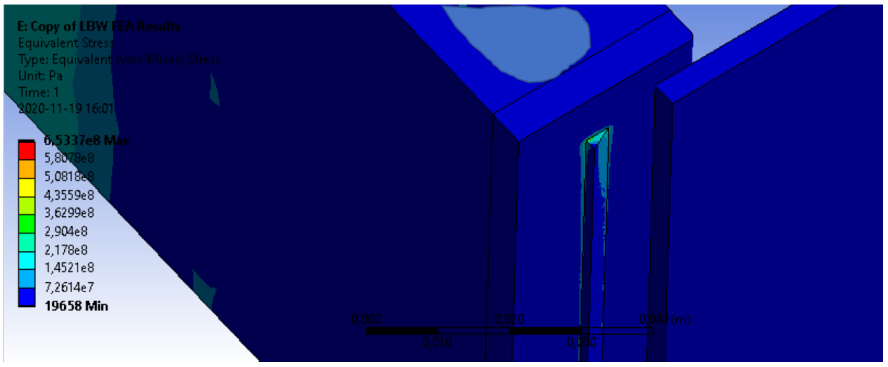

Figure 7.16: View of the LBW FEA model

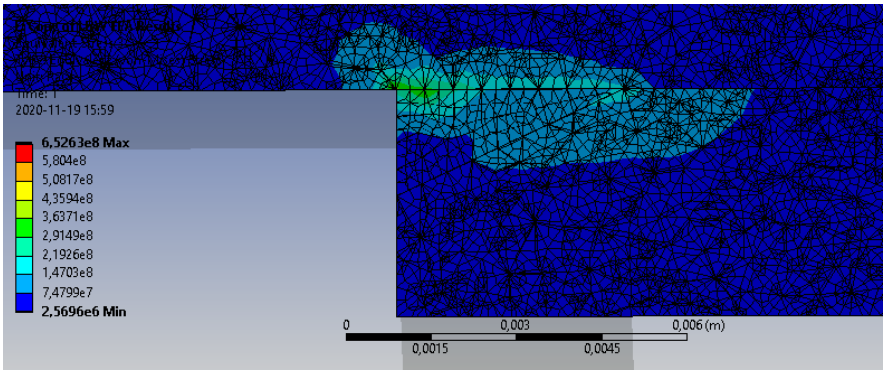

Figure 7.17: Cross section view at the top of the LBW weld bead. Equivalent stress (Von-Mises)

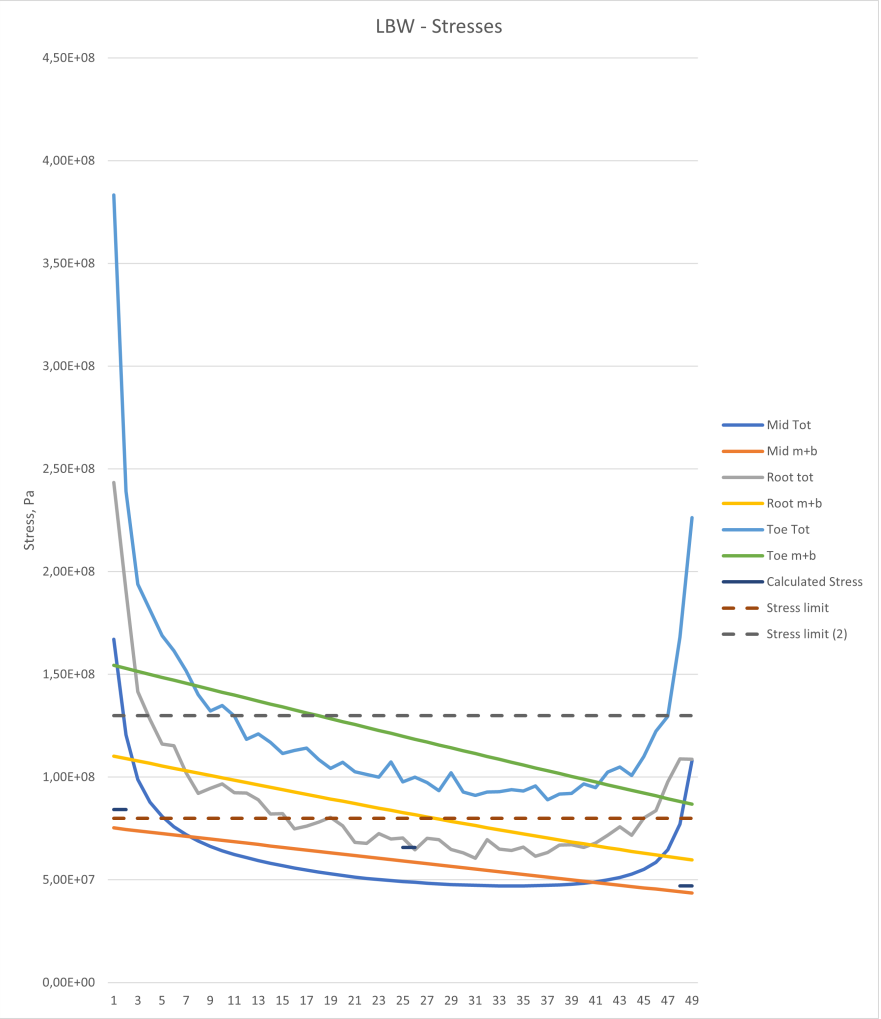

Figure 7.18: Extracted stresses for the LBW weld with element mesh size of 0.25 mm, calculated stresses shown with three dashes for top, mid and bottom of the weld. Stress on the Y-axis in Pa and sample number on the X-axis.

7.5.2 3D model & approximation of a 2D model

To better understand the effect of using a 3D model to compare with the hand calculation, a model of the TIG weld was run with a geometry, more similar to the 2D load case used in the calculations in section 6. Supports are redefined to the corresponding faces and the force is applied on the middle of the side of the endplate. See updated geometry in figure 7.19. A comparison view of the stresses in the initially described load case and in the 2D approximated load case can be seen in figure 7.20.

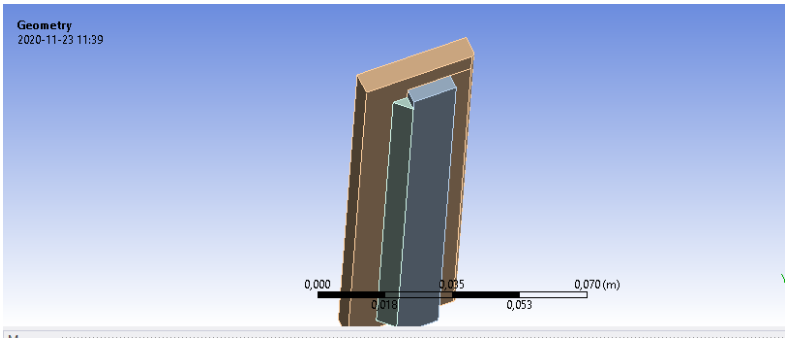

Figure 7.19: TIG model as simplified to be closer to a 2D load case.

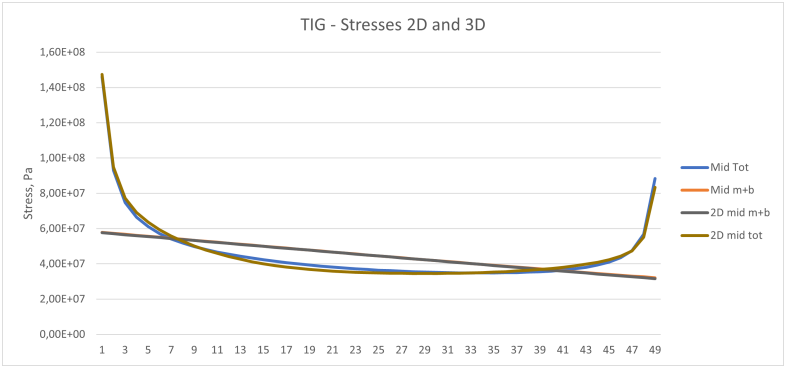

Figure 7.20: Graph of the stresses in position 1, middle of weld body in the 3D loadcase and in the 2D load case approximation as described.

7.6 Discussion FEA results

The high stresses observed in section 7.3.1 for the TIG weld in figure 7.4 show clear indication on singularity errors at the root of the weld with finer mesh size, while the stresses in the middle of the welds show little variation in stress with finer mesh size. Little variation is observed in the middle of the FSW and LBW as well, with the exception of the stress in the coarsest mesh size for the LBW in figure 7.6, which deviates significantly from the results with the two finer meshes.

Singularities as described in section 7.3 are visible for the TIG and FSW in figure 7.11 and figure 7.14 respectively. In both cases these happens co coincide with the weld root and toe, that is, in sharp corners. The very high stress peaks on the top an bottom of the welds in the plotted total stresses in figures 7.12 - 7.18 are also most likely due to singularity errors.

The very high peak stresses that occur at the top and bottom of the welds in the FEA non-linear stress combinations as seen in figures 7.12, 7.15 and 7.18 should also be attributed to singularity errors, and should not be considered accurate.

The stresses as extracted from the middle of the expected shearing plane seem to correlate closest, of the evaluated stresses, with the calculated stress. This is pointing towards that this type of stress extraction method, extracting stresses in the mid-shear plane of the weld, is the most suitable to use to evaluate and compare these different welding methods. This assuming that the assumptions made for the calculations as performed in chapter 6 are reliable. This does not mean that these stresses and this method would be suitable as dimensioning tools. However, there is also very little pointing towards that this method is un-suitable to use as a dimensioning tool for welds, which should be a topic of future research and which due to time-constraints is not a part of this thesis.

For all three suggested welds, the plane shear stresses at the top, peaks above the maximum stress limit as set in chapter 6. The most significant overstepping of this limit is seen in the LBW in figure 7.18, where both the calculated stress and the mid-total (shearing plane stress) crosses the stress limit. However, if the stress limit is at stress limit (2), at 130 MPa as seen in the figure, the

LBW could be the geometry with the highest general margin to the maximum allowed stress.

The results in section 7.5.2 points towards that there is no significant difference between the 3D models and the approximated 2D load case.

Error Sources

As always when analysing and simplifying models, there are a lot of possible different error sources to account for. These will not be explained in detail but some of the most obvious error sources are listed below.

Some error sources include and are not confined to:

- Simplification of boundary conditions
- Simplification of weld bead geometry
- Singularities

The material models in the FEA software is also linear and does not account for any plasticity in the material. This, together with meshing singularities and the unrealistic geometry for the weld beads can lead to unrealistically high stresses.

Chapter 8

Temperature Analysis

8.1 Introduction to Temperature Analysis

8.1.1 Introduction

Predicting temperatures during welding operations can include a vast amount of variables and computation. Material properties change with varying pressure and temperature and boundary conditions are difficult to define. For accurate replication of the welding process, things such as varying specific heat and conductivity should be modelled, as well as the exothermic behaviour of solidification. Accurate thermal models can be very complex and are out of the scope of the work in this thesis. With the goal of comparing these methods against each other, simplifications and introduction of error sources should be made equally for all the welding methods.

In order to get any type of results that are comparable, considering the different nature and physical heating processes of the TIG, FSW and LBW methods, a very simplified model of thermal development simulation should be used, with a limited set of easily controlled variables.

8.1.2 Initial Runs

To understand the heat development, initial finite volume method (FVM) models were set up for all welds respectively. The models were all adiabatic models, with a heat source specified to the specified power of the machines used for the welding processes. This meaning that no cooling what so ever occurs in the model, and that with an infinite amount of time, the temperature also would tend towards infinity. The heat source was specified to a moving point heat source with a radii of 2 mm on the weld geometry, moving with a specified speed up along the weld axis. However, in all models, even though using an otherwise fully adiabatic model, and using the specified power as pure heat generation in the weld, the temperatures reached were very low. This was partially realized as a result of comparison to simulations and testing on heat development that had been provided by the supplier of the FSW weld. These simulations and tests were quite close / accurate to one another and showed much higher temperatures than achieved by the initial runs.

Another part of this was the fact that the maximum temperatures in the initial runs didn't reach the melting point of aluminium, even in the center of the weld.

On a later occasion, it would be realised that the method used by the supplier to specify the power input for the FSW process was based on trial and error by comparing process results and simulation results. Making it difficult to use power input as a baseline for comparison between the different methods.

The method that is described above, is called a constant heat flux method for simulating the temperature history of the welding process.

8.1.3 CIT method

In an article by *Chiocca et al., 2019*, simulating the temperature history of a welding process can be simplified with the use of a constant initial temperature (CIT) method, in which a moving set of elements in the weld bead activates and is set to a specified temperature. This temperature source can then be modeled to travel over the weld geometry with pre-defined process parameters. In their study, they showed that the method of CIT can be used to relatively accurately model the temperature history to geometry close to the welds, as long as a relevant initial temperature is set.

And since, in this report, three different welding methods are to be evaluated, with little information about process parameters, and since it is the temperature history in the proximity of the welds that are to be investigated / compared, a CIT approach to the heat simulations is highly relevant. By using this method, comparing results between the three different welding methods should be more suitable within the demarcations of this report, since the only variables between the simulations should be temperature, geometry and speed.

8.2 Thermal Analysis

The simulations were conducted in a similar fashion as the method explained in section 8.1.3, *CIT Method*. I.e, the weld geometry is modeled and then cells within a certain range are set to a specified temperature, which represents the weld pool. In figure 8.1 the volume with specified temperature can be seen in red. The specification of cells is performed by a defined geometry which acts as the range. Movement is achieved by using a translational movement of the coordinate system of which the geometry / range is specified. The movement after a few iterations of the solution is illustrated in figure 8.2, where the active red elements have translated upwards from it's original position in figure 8.1. Briefly described, a moving portion of the weld is set to the welding temperature.

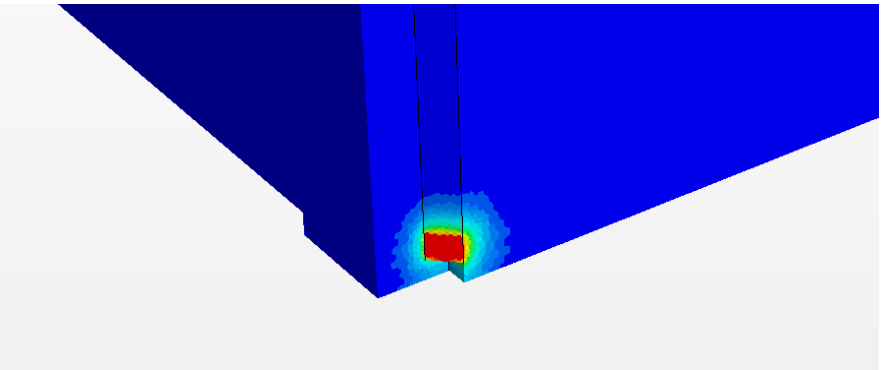

Figure 8.1: Volume of cells set to the specified welding temperature in red.

Temperature Measurement Point - Probe Point

The temperature history is recorded in a specified point for all processes. The measurement point is located on the "cell side" of the sideplate, approximately on the middle height and at a distance of $5mm$ from the endplate. See figure 8.3 for the position of the temperature measuring point. The location of this point can easily be communicated for eventual testing, and fairly easily accessed by a thermocouple.

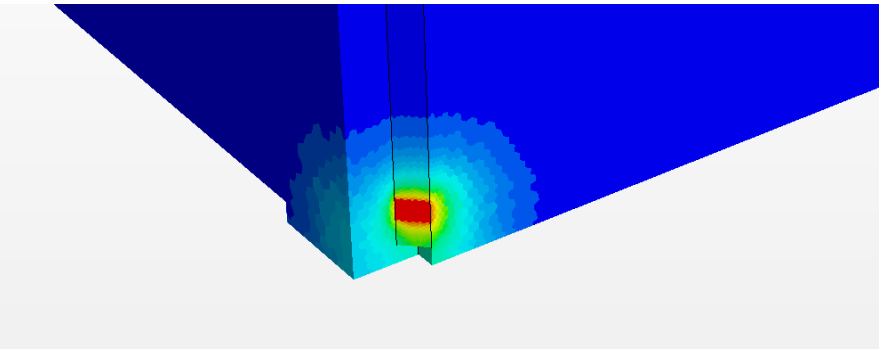

Figure 8.2: Translated volume of cells set to the specified welding temperature in red.

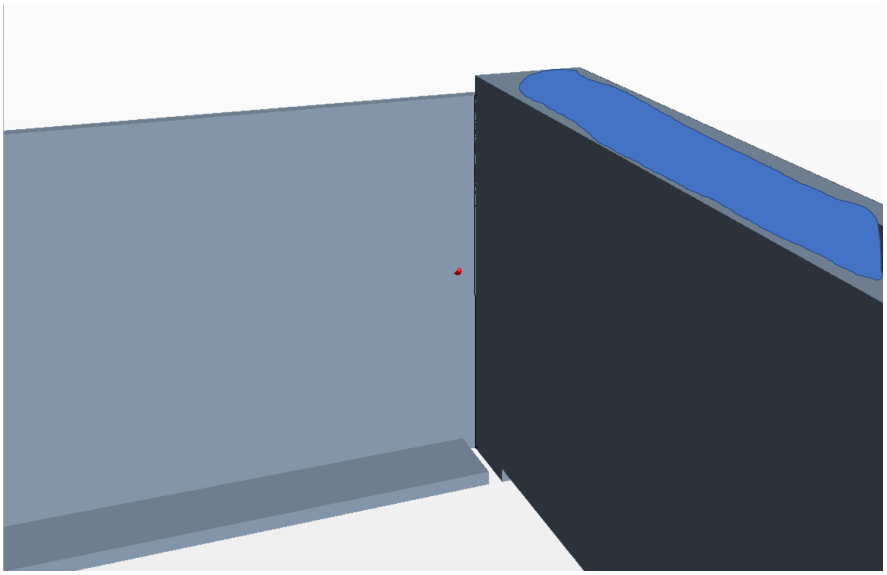

Figure 8.3: Point of temperature measurement

Material Parameters

The material properties used for all three models are identical and static, not temperature dependent. No special regard is taken for the energy in phase change, since the material model is solid. The used properties are at room temperature. These are simplifications and not including the energy in phase change could be a potential error source. However, this could possibly be countered by the fact that using a geometric range which is close to the weld pool size should to a degree compensate for the exothermic solidification.

Table 8.1: Properties used for the temperature development simulations

Density	ρ	2702	kg/m^3
Specific heat	c_p	901	$J/kg-K$
Thermal Conductivity	λ	200	$W/m-K$

Process Parameters

The geometry and process speed can be defined relatively easily, but a temperature for this type of simulation is usually adapted as a result of testing, trial and error, which could compensate for some of the errors introduced by the disregarded material parameters and properties. However, this is not possible in this case. Instead, temperatures will be approximated by using the liquidus or solidus temperatures of the weld bead alloy depending on weld process type. This naturally results in a potentially large error source.

TIG Thermal Analysis

A cad representation of the translating volumetric heat source is shown in figure 8.4

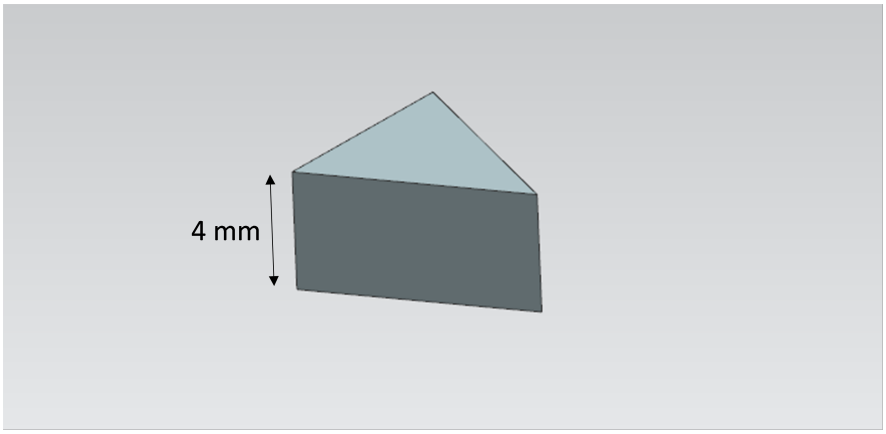

Figure 8.4: CAD representation of volumetric heat source for the TIG weld

The liquidus temperature of the filler material *5356* is used as the *Weld pool temp* as specified in table 8.2.

Table 8.2: Values used for TIG temperature simulation

Translational Speed	4.5	mm/s
Weld pool temp	635	$\deg C$
Weld length	100	mm
Geometry height	4	mm

A view of the TIG temperature simulation 1 second into the process can be seen in figure 8.7, and the temperature history at the probe point can be seen in figure 8.8

FSW Thermal Analysis

A cad representation of the translating volumetric heat source is shown in figure 8.5

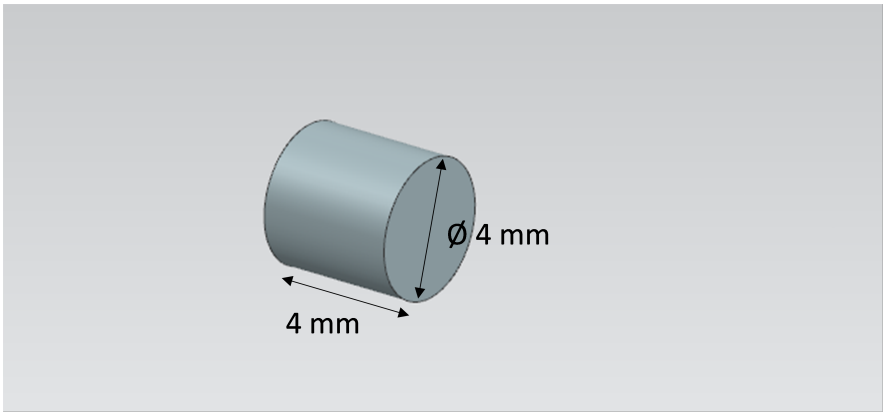

Figure 8.5: CAD representation of volumetric heat source for the FSW weld

Since the temperature in a friction stir weld stabilizes at around the solidus temperature of the base material, see section 3.4, the solidus temperature of the base material *6060* is used as the *Stir zone temp* as specified in table 8.3. For the FSW, the *Geometry height* in table 8.3 is defined as the diameter as shown in figure 8.5.

Table 8.3: Values used for FSW temperature simulation

Translational Speed	12.5	mm/s
Stir zone temp	620	$\deg C$
Weld length	90	mm
Geometry height	4	mm

A view of the FSW temperature simulation 1 second into the process can be seen in figure 8.9, and the temperature history at the probe point can be seen in figure 8.10

LBW Thermal Analysis

A cad representation of the translating volumetric heat source is shown in figure 8.6

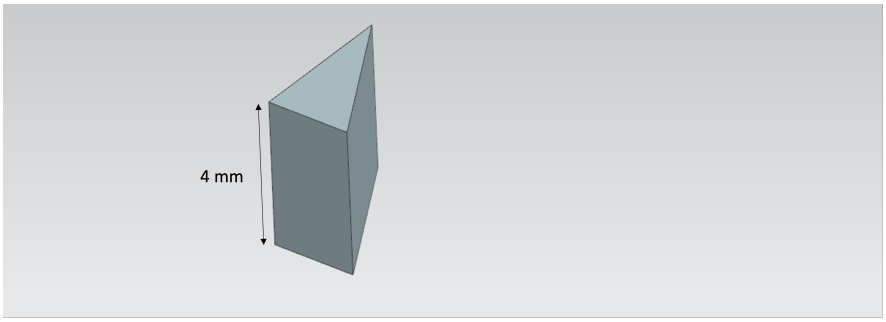

Figure 8.6: CAD representation of volumetric heat source for the LBW weld

The liquidus temperature of the base material in the sideplate *5754* is used as the *Weld pool temp* as specified in table 8.4.

Table 8.4: Values used for LBW temperature simulation

Translational Speed	66	mm/s
Weld pool temp	645	$\deg C$
Weld length	100	mm
Geometry height	4	mm

A view of the LBW temperature simulation 1 second into the process can be seen in figure 8.11, and the temperature history at the probe point can be seen in figure 8.12

8.3 Results

TIG

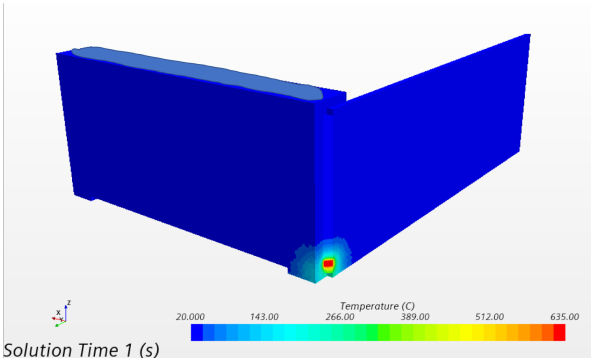

Figure 8.7: TIG: Heat map after 1 second of welding process

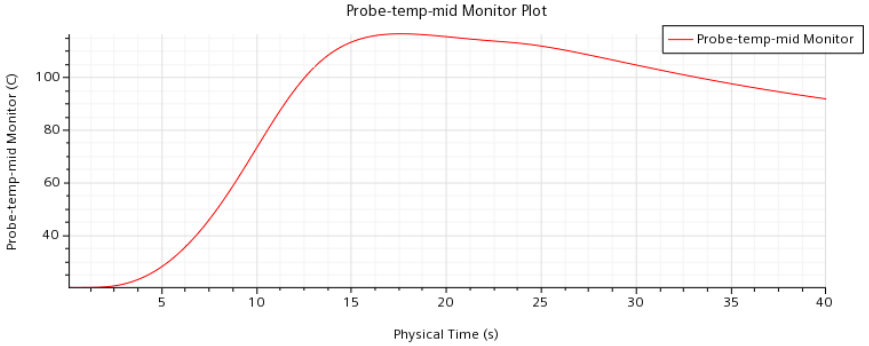

Figure 8.8: TIG: Temperature history at the probe point. Temperature vs time. Max temp reached approx 116 deg C

FSW

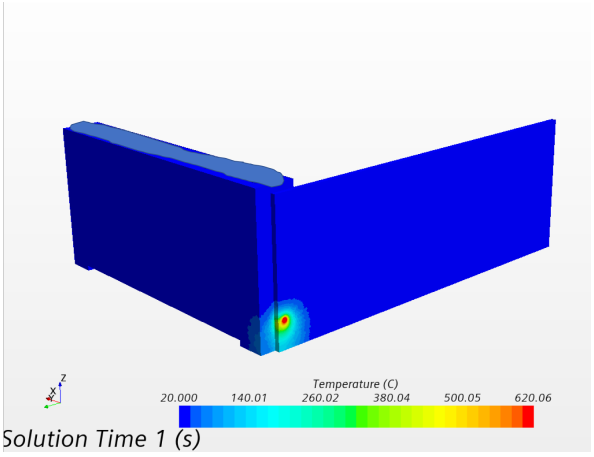

Figure 8.9: FSW: Heat map after 1 second of welding process for the FSW

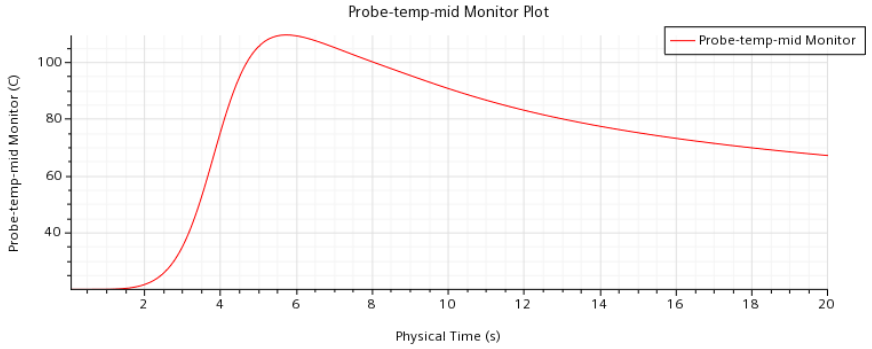

Figure 8.10: FSW: Temperature history at the probe point. Temperature vs time. Max temp reached approx 109 deg C

LBW

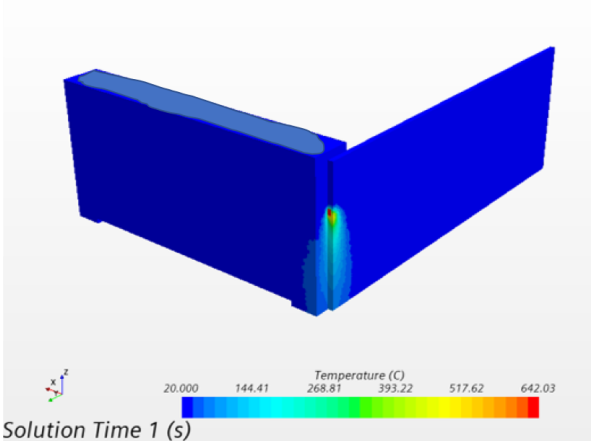

Figure 8.11: Heat map after 1 second of welding process for the LBW

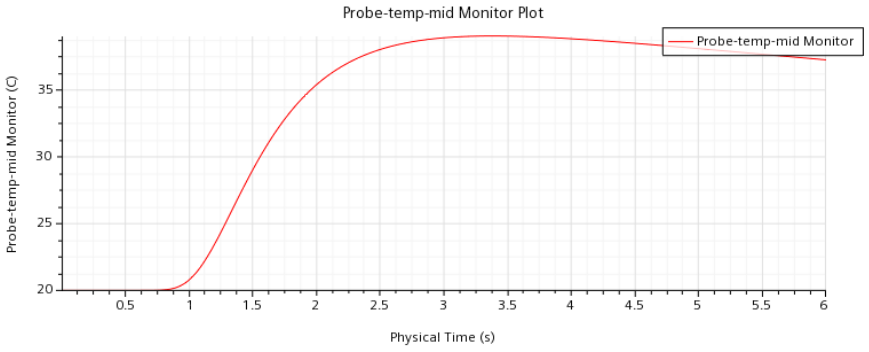

Figure 8.12: LBW: Temperature history at the probe point. Temperature vs time. Max temp reached approx 39 deg C

8.4 Measured Temperatures of Welds

In order to validate / compare the results of the temperature simulations in figures 8.8, 8.10 and 8.12 in section 8.3, maximum welding process temperatures were obtained from outsourced trials of the welding processes.

TIG

TIG temperature information was found using only temperature sensitive stickers that max out at around 110 deg C and might therefore be unsuitable for comparison.

- Sticker close to endplate. No specified distance.
- Max measured temperature > 110 deg C

FSW

FSW temperature data was provided by *Hydro Extrusion Sweden AB* for a similar setup as evaluated for the weld used in section 8.3. Where temperature was measured with thermocouples. See figure 8.13. The staring temperature of the testing and the environment wasn't identical to the simulated starting temperature, and the sampled testing data came as a raw stream without comments. The staring temperature of the simulations were therefore offset to match the first recorded temperature in the tests. Time alignment was achieved by time aligning the maximum temperatures from the simulated and tested data.

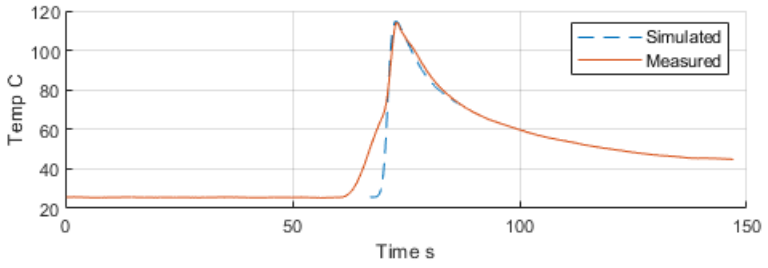

Figure 8.13: Temperature simulation of FSW and Measurements as provided by *Hydro Extrusion Sweden AB*: Temperature history at the probe point. Max measured temp reached approx 114 deg C. Simulated start temperature corrected by offset to similar start temp. Temperature peaks are time aligned.

- Thermocouple placement - 7 mm from endplate.
- Max measured temperature 114 deg C

LBW

LBW temperature data was provided by *Permanova Lasersystem AB* for a setup with similar geometry used in section 8.3, but at at half speed. In order to get data suitable for comparison, a temperature analysis for the LBW is run analogously section 8.2, but at a traversing speed of 33 mm/s instead of 66 mm/s. See figure 8.14. The staring temperature of the testing and the environment wasn't identical to the simulated starting temperature, and the sampled testing data came as a raw stream without comments. The staring temperature of the simulations were therefore offset to match the first recorded temperature in the tests. Time alignment was achieved by time aligning the maximum temperatures from the simulated and tested data.

Additional Temperature Simulation for LBW

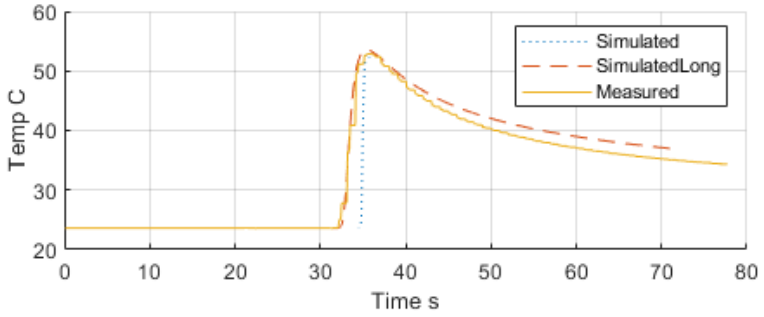

Figure 8.14: Half speed temperature simulations of LBW and Measurements as provided by *Permanova Lasersystem AB*: Temperature history at the probe point. Max measured temp reached approx 53 deg C. Simulations have corrected starting temperatures by offset. Temperature peaks are time aligned.

Simulated temperature is simulated with identical setup as in 8.3, and *SimulatedLong* has a larger solution step to achieve a faster solution time.

- Thermocouple placement - 6 mm from endplate.
- Max measured temperature 53 deg C

8.5 Sensitivity Analysis

A sensitivity analysis was performed for the FVM process parameters, *Translational speed*, *weld pool temperature* and for the *geometry height*. In tables 8.5, 8.6 and 8.7 the sensitivities depending on the process parameters can be seen respectively. Sensitivity is calculated by varying speed, temperature and geometry height by a percentage, and then comparing the change in maximum temperature at the probe point to the baseline.

Table 8.5: Sensitivities of the TIG FVM

TIG Sensitivities	
Variable	*Change in %*
Speed + 5 %	-2.15
Speed - 5 %	+2.29
Temperature + 5 %	+4.14
Temperature - 5 %	-4.14
Geometry + 5 %	+1.39
Geometry - 5 %	-1.37

Table 8.6: Sensitivities of the FSW FVM

FSW Sensitivities	
Variable	*Change in %*
Speed + 5 %	-2.12
Speed - 5 %	+2.27
Temperature + 5 %	+4.08
Temperature - 5 %	-4.08
Geometry + 5 %	+2.51
Geometry - 5 %	-2.45

Table 8.7: Sensitivities of the LBW FVM

LBW Sensitivities	
Variable	*Change in %*
Speed + 5 %	-1.38
Speed - 5 %	+1.5
Temperature + 5 %	+2.44
Temperature - 5 %	-2.44
Geometry + 5 %	+1.09
Geometry - 5 %	-1.11

8.6 Evaluation of results

Discussion

The FVM simulations as performed above do show a possibility to be used as part of a design methodology after calibration. In the current state of the simulation models however, the only suitable use is for a very rough comparison between the welding methodologies.

Both the FSW and LBW test and simulation data show promising correlation and is pointing towards that the models used can work as a development tool before testing and validation.

The sensitivity analysis performed in section 8.5, also points towards a reasonable stability of the simulations.

It should be clear both after simulation and measurement that the LBW design suggestion is by far the coolest welding method, *literally*, of the three and should be considered as a valid design choice as of the maximum temperature requirement stated in section 4.

Error sources

There are a lot of possible error sources in the simulations above in comparison the actual welding processes. Many of the errors however, should be constant over the three analysed weld suggestions, although their impact may vary.

Some of the most obvious error sources include:

- The models are all simplified to adiabatic conditions
- Static parameters for materials, meaning no regards for phase-change, which could lead to lower probing temperature since there is no exothermic solidification. Static values for specific heat and conductivity might also lead to deviations to real behaviour.
- Chosen size of temperature source
- Connection between the touching areas between endplate and sideplate

are fully conductive, which also might lead to lower probing temperatures.

- Choice of weld pool temperature is quite arbitrary
- TIG welding puts a lot of heat in the base metal as well, which is not accounted for

The measured TIG trial temperature data did not show any specific temperatures, and since the TIG weld was performed manually, no process parameters were clearly defined. However, as TIG welding usually puts a lot of heat energy into the base material relative to the heat energy in the weld bead, especially as compared to the other investigated welding methods, the temperature of the TIG weld calculation should be, relative the other welding methods, quite unconservative i.e. the actual process temperature of the TIG weld is expected to be higher than simulated.

In the sensitivity analysis performed in section 8.5, a major error source for the validity of the *Geometry* variable could be due to the size of the meshed elements. Elements are activated if the center of the element is within a specified distance from the source, and thus errors could arise with a large element size and a small change in distance. To clarify, a 5 % increase of the "activation range" might not be sufficient to reach 5 % more cells in a specific instance. Add here the fact that these simulations are performed in discrete time-steps.

Chapter 9

Conclusions, Recommendations & Further Research

9.1 Results

From the calculations, FEA and FVM, out of the three investigated welding joint solutions, the LBW is the most promising solution with regards to the requirements stated in section 4.2.1. That is, the LBW shows the highest safety margin in terms of the temperature requirements. However, in order to safely determine that the LBW is passing the strength requirements, the weld characteristics need to be validated by testing.

9.2 Other Concerns

The fatigue life is not at all evaluated in this report, and due to the discussed hot cracking characteristics of the suggested LBW, fatigue life is of extra concern.

Since battery modules such as the one in this report can be subject to large scale production, the tact time of each weld is an important factor for industrialisation purposes. Even though not discussed much in this report, it is

mentioned that LBW can be a fast and automated process, in relation to TIG welding.

Further, there are many more aspects when it comes to large scale productions, such as risk assessments of failures in the process, and process dependability. All of which, amongst many more, should be taken into account.

9.3 Possible Designs

LBW with filler material

A problem with using the 5754 alloy as sideplate alloy is that it is harder to extrude the sideplate profile with it, compared to the 6060 alloy. A possible solution to this problem is to use the 6060 alloy on both sideplate and endplate while performing the LBW fillet weld as investigated in chapter 5, but with the use of a filler wire. LBW of 6xxx series alloys are commonly performed within the automotive industry with filler materials as mentioned by (*Zhao et al., 1999*). Using a filler from the 4xxx series could increase the Si alloying content of the weld pool well above 2 % , and thereby lower the hot-cracking sensitivity as shown in figure 3.2, in section 3.3. This is a common solution for applications where a 6xxx-series alloy needs to be welded to itself, that however does increase cost and complexity and potentially increase weld process time.

With the use of a filler alloy such as 4043, the strength of the LBW weld, could according to *"Eurocode 9: Design of aluminium structures", 2007, table 8.8*, have a weld strength of $f_w = 150$ MPa, which is significantly higher than the initial assumption and the speculation of $f_w = 80$ and $f_w = 130$ MPa respectively.

The overall process temperature as investigated in section 8.2 shows a promising safety margin, to which a slower LBW process would be feasible while still passing the maximum process temperature requirement of 80 deg C as stated in section 4.2.1.

9.4 Closing Remarks

As closing remarks, the conclusions of this reports are to further investigate the use of LBW for welding of the prismatic module frame. It shows a promising safety factor in terms of temperature development and should be a possibly fast and strong welding method.

Needless to say, there are many more things to consider, when choosing a welding method for use in a mass produced product, that have not been considered in this work.

It is my hope that the work and findings in this thesis will be of value to the team at northvolt in the work of designing a prismatic cell module.

References/Referenser

Barai, A., Tangirala, R., Uddin, K., Badin, J., Guo, Y., McGordon, A., & Jennings, P. (2017). The effect of external compressive loads on the cycle lifetime of lithium-ion pouch cells. *Journal of Energy Storage*, *13*, 211–219. https://doi.org/10.1016/j.est.2017.07.021

Berg, P., Soellner, J., Herrmann, M., & Jossen, A. (2020). Structural dynamics of lithium-ion cells—part ii: Investigation of large-format prismatic cells and method evaluation. *Journal of Energy Storage*, *28*, 101246. https://doi.org/10.1016/j.est.2020.101246

Chiocca, A., Frendo, F., & Bertini, L. (2019). Evaluation of heat sources for the simulation of the temperature distribution in gas metal arc welded joints. *Metals*, *9*, 1142. https://doi.org/10.3390/met9111142

Colligan, K. (2010). 6 - solid state joining: Fundamentals of friction stir welding (X. Sun, Ed.). In X. Sun (Ed.), *Failure mechanisms of advanced welding processes*. Woodhead Publishing. https://doi.org/10.1533/9781845699765.137

Eurocode 9: Design of aluminium structures. (2007).

Forsman, T. (2000). Laser welding of aluminium alloys.

Jae Hyun LeeH, S. A., yang Mok Lee. (2003). Battery dimensional changes occurring during charge/discharge cycles—thin rectangular lithium ion and polymer cells. *Journal of Power Sources*, *119 - 121*, 833–837. https://doi.org/10.1016/S0378-7753(03)00281-7

Ki-Yong Oh, B. I. (2017). A phenomenological force model of li-ion battery packs for enhanced performance and health management. *Journal of Power Sources*, *365*, 220–229. https://doi.org/10.1016/j.jpowsour.2017.08.058

Lee, J.-M., Seo, J.-K., Kim, M.-H., Shin, S.-B., Han, M.-S., Park, J.-S., & Mahendran, M. (2010). Comparison of hot spot stress evaluation methods for welded structures. *International Journal of Naval Architecture and Ocean Engineering*, *2*(4), 200–210. https://doi.org/10.2478/IJNAOE-2013-0037

Northvolt. (2020). https://www.northvolt.com/

Oh, K.-Y., & Epureanu, B. I. (2016). A novel thermal swelling model for a rechargeable lithium-ion battery cell. *Journal of Power Sources*, *303*, 86–96. https://doi.org/10.1016/j.jpowsour.2015.10.085

Oh, K.-Y., Siegel, J. B., Secondo, L., Kim, S. U., Samad, N. A., Qin, J., Anderson, D., Garikipati, K., Knobloch, A., Epureanu, B. I., Monroe, C. W., & Stefanopoulou, A. (2014). Rate dependence of swelling in lithium-ion cells. *Journal of Power Sources*, *267*, 197–202. https://doi.org/10.1016/j.jpowsour.2014.05.039

P. Kah, E. H., & Martikainen, J. (2010). Investigation of hot cracking in the welding of aluminium alloys (6005 & 6082). https://doi.org/10.13140/2.1.4215.6324

Pradeep Sensharma, J. H., Matthew Collette. (2010). Effect of welded properties on aluminum structures.

Tibnor. (2020). *Aluminium: Teknisk data*. https://www.tibnor.se/

Zhao, H., White, D., & Debroy, T. (1999). Current issues and problems in laser welding of automotive aluminum alloys. *International Materials Reviews*, *44*, 238–266. https://doi.org/10.1179/095066099101528298

Appendix A

appendicesA

A.1 Project Plan

The project plan for this thesis can be seen in figure A.1.

Not many thesis projects goes exactly as planned, and this thesis neither. Testing of the welds was eliminated from the project due time constraints and internal discussion about what samples could be manufactured. Instead, thermal analysis of the welding process was added as it became clear that the temperatures reached during the welding processes were of concern.

A rough estimation of time spent can be seen in figure A.2

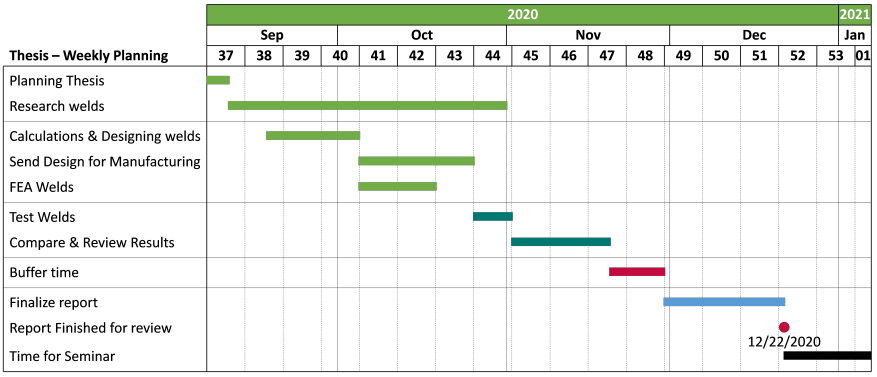

Figure A.1: Project Plan, Gantt chart.

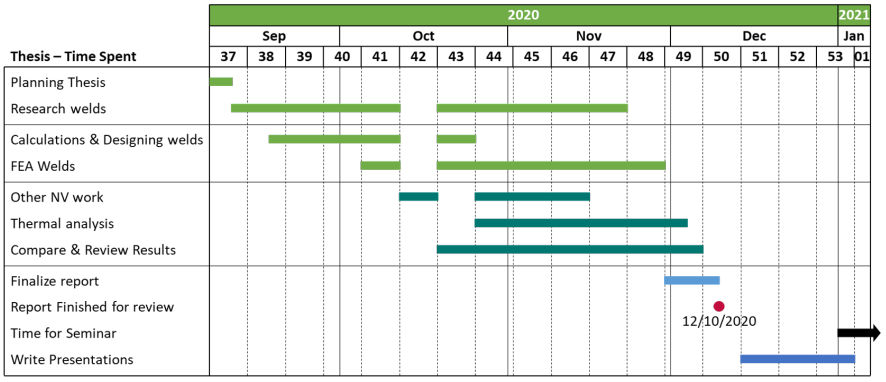

Figure A.2: Time Spent, Gantt chart.

Appendix B

PullJig

B.1 Pull Test Jig Design

During my second week of work, I took the task upon myself to re-design the pull test jig, to make it cheaper to manufacture and to optimize the load-case in order to reduce the bending moment on a few parts.

The first version of the pull test jig can be seen in figure B.1 and figure B.2. There were some concerns expressed of the loading of this jig. One of the concerns were of the load cell not being centered on the weld, which would result in high bending stresses on the bracket that pulls against the module frame.

The second version, *the first version I designed*, can be seen in figure B.3 and figure B.4.

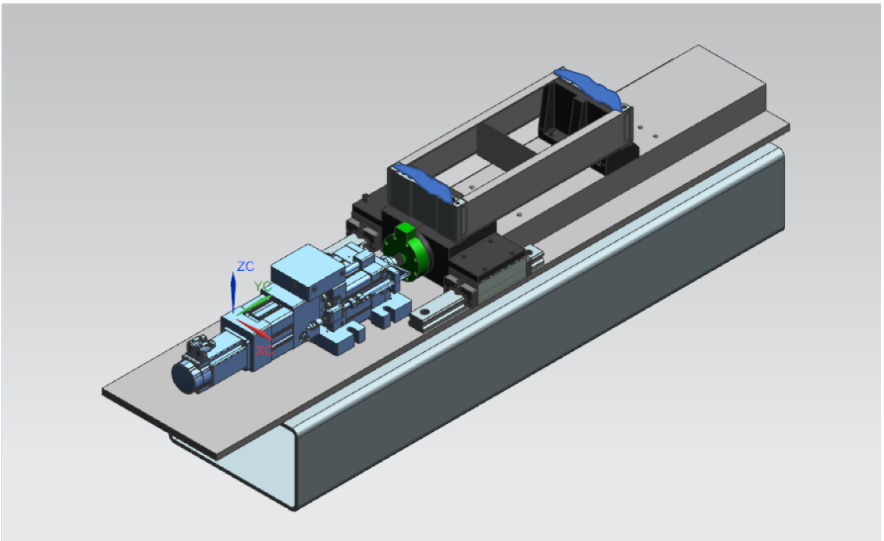

Figure B.1: Isometric view of the first version of the Pull test jig, that was presented during the beginning of the thesis.

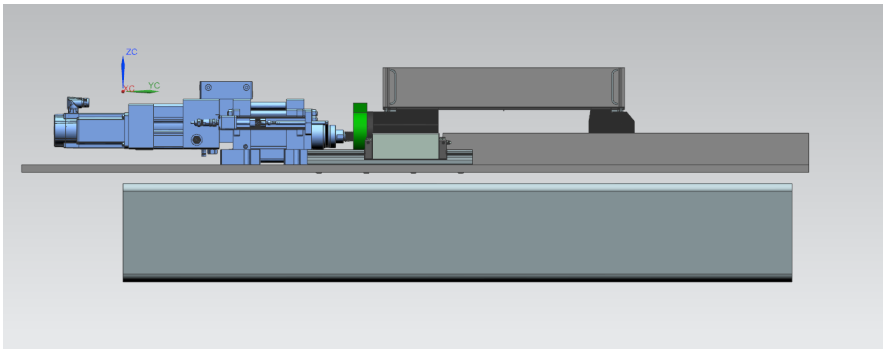

Figure B.2: Right view of the first version of the Pull test jig, that was presented during the beginning of the thesis.

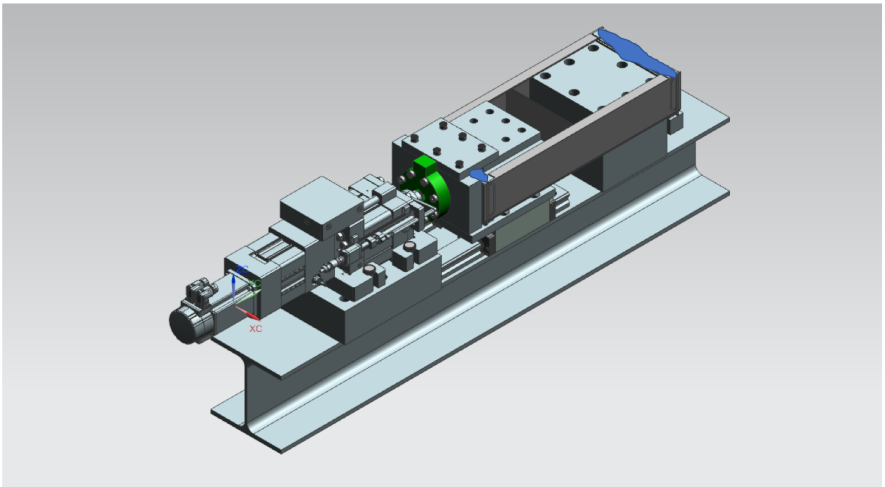

Figure B.3: Isometric view of version 2 of the designed Pull test jig

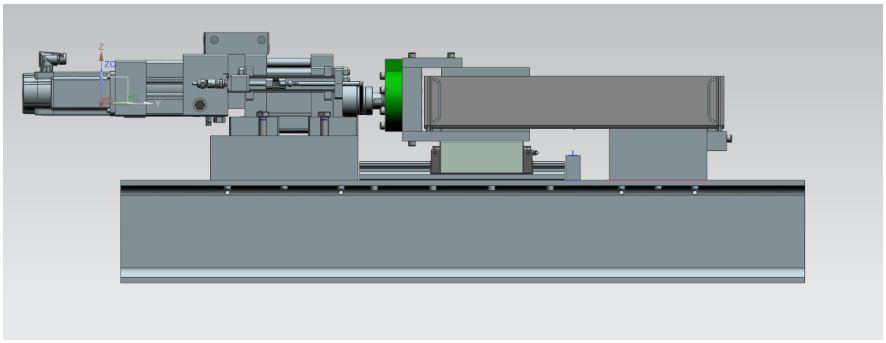

Figure B.4: Right view of version 2 of the designed Pull test jig

Appendix C

Initial weld calculations

In this appendix, all the first initial calculations is performed on the three different welds. This is done to get a feel for the methods and to quickly compare their relative strengths. In these calculations the force is approximated to be reacted in the welds as a pure normal force and no torque. All following calculations are simple approximations and should not be treated otherwise.

C.1 Initial Weld Calculations

The material data used in this chapter can be found in table C.1. Note that in this chapter, the material data is sourced elsewhere, and the $R_{p0,2}$ strength is used in contrast to the values stated in Eurocode 9.

Table C.1: Material data used for initial weld calculations

Where	*Material*	*Type*	*Value*
TIG			
Side plate	Aluminium 6060 F22 T6	$R_{p0,2}$	150 MPa
End Plate	Aluminium 6060 F22 T6	$R_{p0,2}$	150 MPa
Filler Rod	AluTIGMg5 (5356)	$R_{p0,2}$	125 MPa
FSW			
Side plate	Aluminium 6060 F22 T6	$R_{p0,2}$	150 MPa
End Plate	Aluminium 6060 F22 T6	$R_{p0,2}$	150 MPa
Weld Zone	Strength is 80 % of base material	$R_{p0,2}$	120 MPa
Laser			
Side plate	5754 H22	$R_{p0,2}$	130 MPa
End Plate	6060 F22 T6	$R_{p0,2}$	150 MPa
Weld Zone	Strength is 70 % of base material	$R_{p0,2}$	91 MPa

C.1.1 Initial TIG Weld Calculations

The initial TIG weld design is an overlapping joint of full length along the side plate (see figure C.1) , where the thickness of the side plate sets the maximum bound of the a-dimension. As the a-dimension is simplified as in figure C.2, the maximum a-dimension is described in relation to the plate thickness t as in equation C.1:

$$a_{max} = \sqrt{\frac{t^2}{2}} \tag{C.1}$$

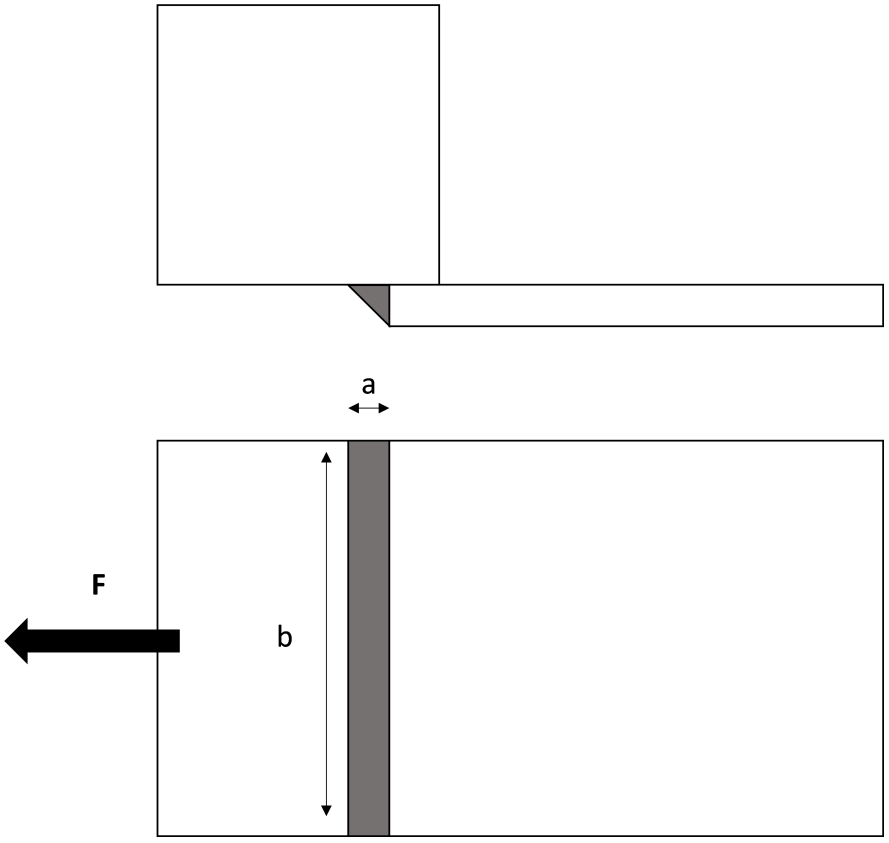

Figure C.1: Geometry of the initially calculated TIG weld

As initial calculation, the necessary a-dimension of the weld is calculated. First a free body diagram of the weld is displayed in figure C.2.

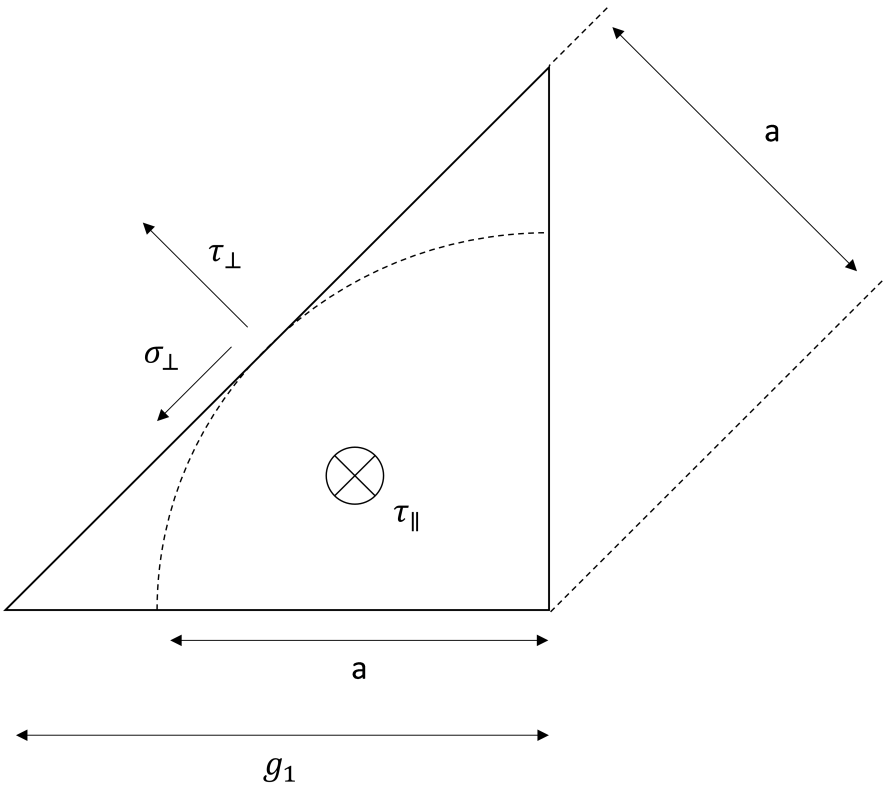

Figure C.2: Free body diagram of a TIG weld

For the weld, the conservative approximation is made such that the a-dimension is projected down as in figure C.2. The stress can be described according to Von-Mises as in equation C.2

$$\sigma_{vm} = \sqrt{\sigma_\perp^2 + 3 \cdot (\tau_\perp^2 + \tau_\parallel^2)} \tag{C.2}$$

Another conservative assumption is made that the the join reacts purely in shear stress. Thus, equation C.2 can be simplified into such in equation C.3

$$\sigma_{vm} = \tau_\parallel \cdot \sqrt{3} \tag{C.3}$$

And the force can be described as

$$F = \tau_{\parallel} \cdot A \tag{C.4}$$

Where A is the area of the weld, and is described as

$$A = a \cdot b \tag{C.5}$$

With equation C.3, C.4 and C.5, the a-dimension for a can be solved for as in equation C.6.

$$a = \frac{F \cdot \sqrt{3}}{\sigma_{vm} \cdot b} \tag{C.6}$$

With the force $F = 15$ kN and $\sigma_{vm} = 125$ MPa as taken from the properties of the filler material AluTigMg5[1] and the length $b = 100$ mm equation C.6 gives that $a = 2.0785$ mm. With the restriction of the side plate being 4 mm thick, 2.83 mm is the higher bound of the a-dimension in accordance with equation C.1. And since the load-case already includes a safety factor, it should be possible to design a TIG weld that withstands the required loads in regards to the shearing stresses. However, this calculation has taken no regard for any other failure modes.

Table C.2: Values for the initial TIG weld

Variable	*Value*
F	15 kN
b	100 mm
σ_{vm}	125 MPa
t	4 mm
a_{max}	2.83 mm
a	2.0785 mm

[1] https://elga.se/product/alutig-mg5/

Veryfying that the endplate of the construction still holds as a result of the HAZ weakening. The strength of the HAZ can be approximated by the HAZ-factor. ("Eurocode 9: Design of aluminium structures", 2007)

The endplate has a cross sectional area of about $0.0004m^2$, and with a force of $15kN$, the resulting stress is $37.5MPa$.

If the end-plates strengths is reduced to only 43 % as a result of the HAZ ("Eurocode 9: Design of aluminium structures", 2007),the yielding strength of the base material would be $64.5MPa$. It is clear that the profile holds.

C.1.2 Initial FSW Calculations

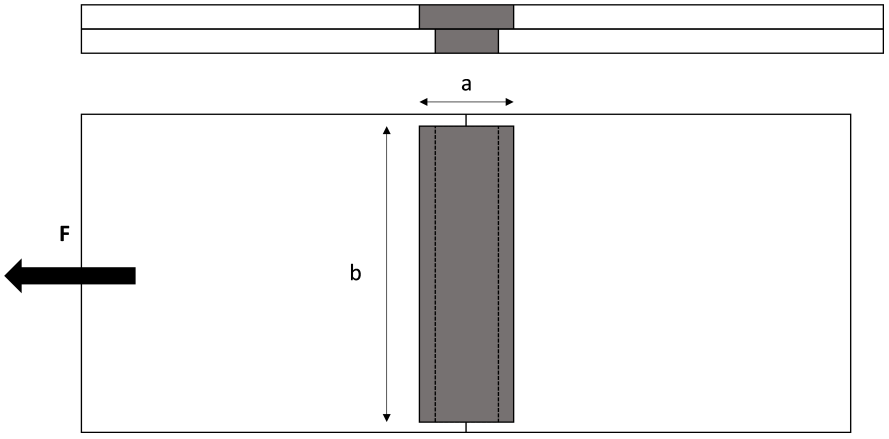

Figure C.3: Geometry of the initially calculated FSW weld

The first calculation on the FSW is performed similarly to the TIG weld calculations in section C.1.1. Since FSW does not require any filler material, only the material parameters of the end plate and side plate are required. However, for this calculation, the tensile strength of the welded area will be approximated to have only 80 % of the base materials tensile strength. [2]

The required a-dimension can be calculated with the same equation C.6, with the parameters from table C.3. As a consequence of the geometry of the FSW head, for the initial calculations, it is approximated that around $2cm$ will be subtracted from the height of the side plate for the weld. This to account for entry and exit of the FSW head and other possible geometry obstruction.

[2] https://www.riftec.de/en/friction-stir-welding.html

Table C.3: Values for the initial FSW weld

Variable	*Value*
F	15 kN
b	80 mm
σ_{vm}	120 MPa
a	2.706 mm

The a-dimension is not restricted by the material thickness of the side plate as the TIG weld option, but instead restricted only by the thickness of the end plate. This will most likely not be an issue.

C.1.3 Initial Laser Welding Calculations

As the 6060 aluminium alloy has a relatively low Si content

Even though a standard is hard to find, testing results have previously shown some indications of the mechanical properties of laser welds in aluminium. Forsman, 2000 70 % of the base materials yield strength can be expected for a successful joint.

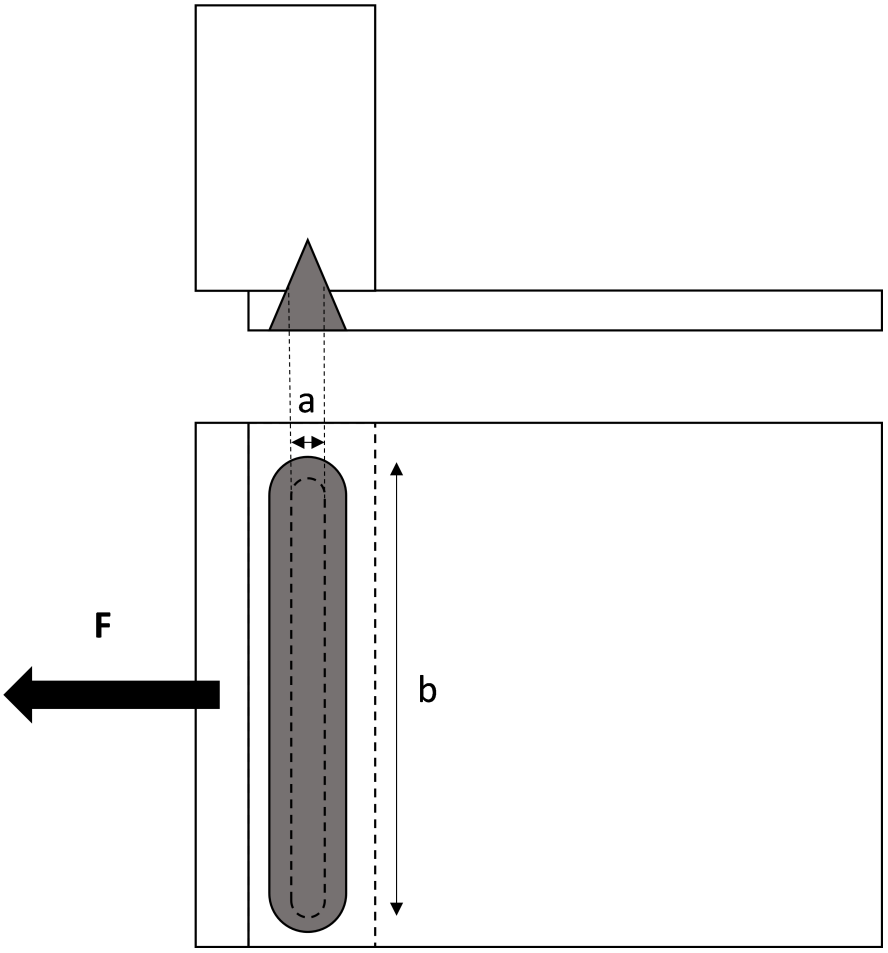

Figure C.4: Geometry of the initially calculated Laser weld

Table C.4: Values for the initial Laser weld

Variable	*Value*
F	15 kN
b	90 mm
σ_{vm}	91 MPa 70% of 130 MPa
a	3.17 mm

Table C.5: Material data used for initial weld calculations. Data retrieved from *Tibnor, 2020*

Alloy	*Yield Strength*	*Alloying composition*	*Total alloying %*
6060 F22 T6	150 MPa	Si 0.4; Mg 0.5; Fe 0.2	1.1 %
6082 T6	260 MPa	Si 1.0; Mg 0.85; Mn 0.65	2.5 %
5754 H22	130 MPa	Mg 3.1; Mn 0.5; Cr 0.3	4.2 %

Appendix D

Initial FEA

D.1 Initial FEA

Initial FEA was carried out on all models. A weld dimension at $2mm$ was used for all welding methods. Again as a baseline.

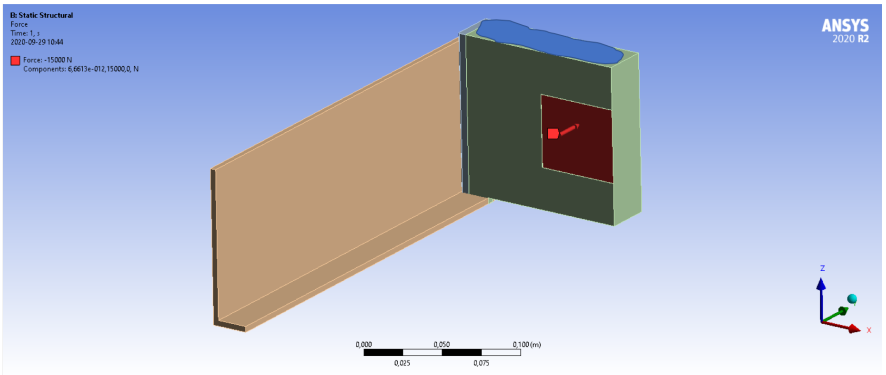

Figure D.1: 15 kN force spread out as pressure over the red surface

The end plate and side plate as used in this section are cut in half, as the other side is mirrored. The FEA model can then use less elements and less

processing power to solve the problem efficiently.

A force of $15kN$ is applied to a specified surface as a pressure. This can be seen in figure D.1.

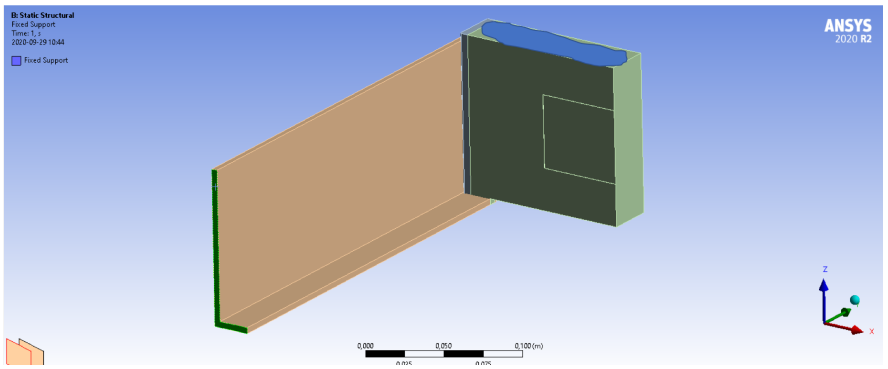

Figure D.2: Fixed support on side plate end

In figure D.2 and in figure D.3 the frictionless support an the fixed support can be seen.

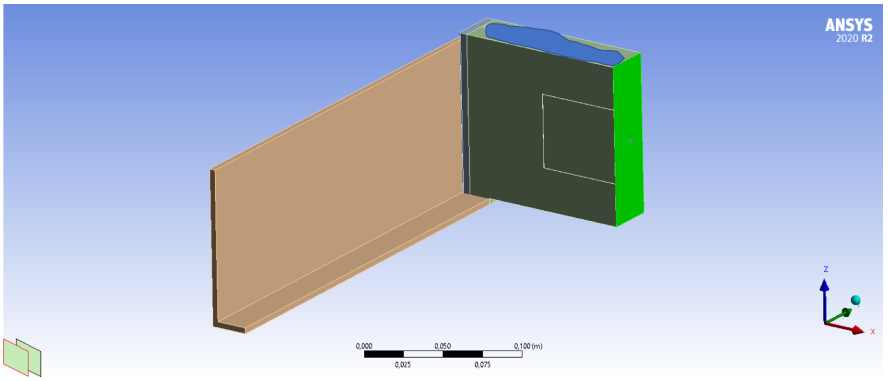

Figure D.3: Frictionless support on end plate

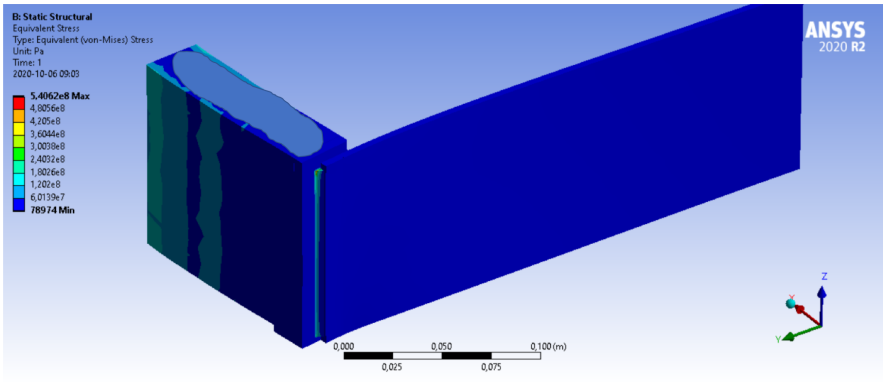

Figure D.4: Initial TIG weld FEA

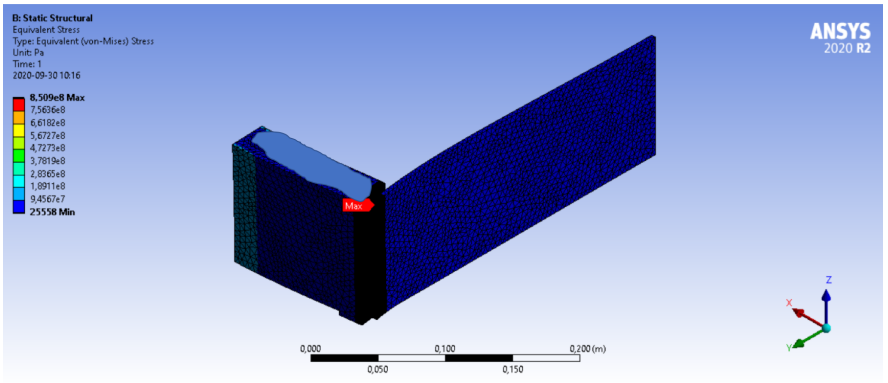

Figure D.5: Initial FSW FEA

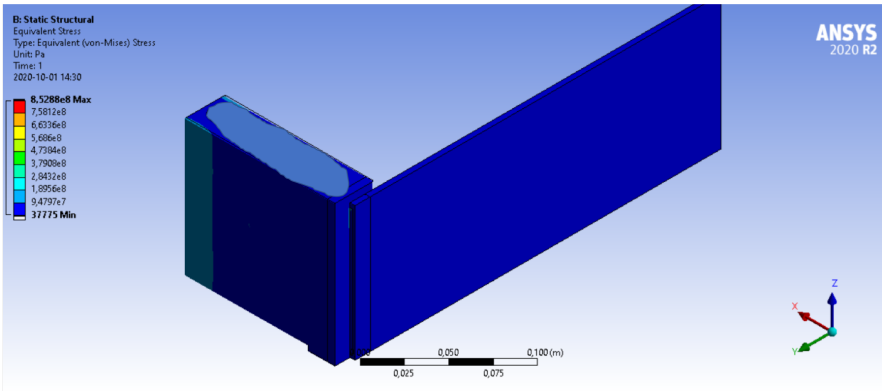

Figure D.6: Initial LBW FEA

From these initial welding calculations, it is clear that the highest stresses are found on the top side of the weld. This is a result of a bending moment, since the force is not applied in line with the middle of the weld.

Appendix E

6082 LBW pull tests

E.1 6082 LBW Sample tests

LBW Samples were tested with aluminium 6082 T6 alloy. The geometries or welds were provided in which I helped out with analysing the welds and testing their failing strength. 6082 generally has an M_gS_i content of around 1.4 % and 6060 M_gS_i content of around 1 %, both close to the peak of the crack sensitivity curve as shown in section 3.3, figure 3.2. Therefore this section will regard these alloys as having similar crack-sensitivity.

6082-6082

The welded sample of 6082 to 6082 had large cracks formed along the welds, as can be seen in figure E.1.

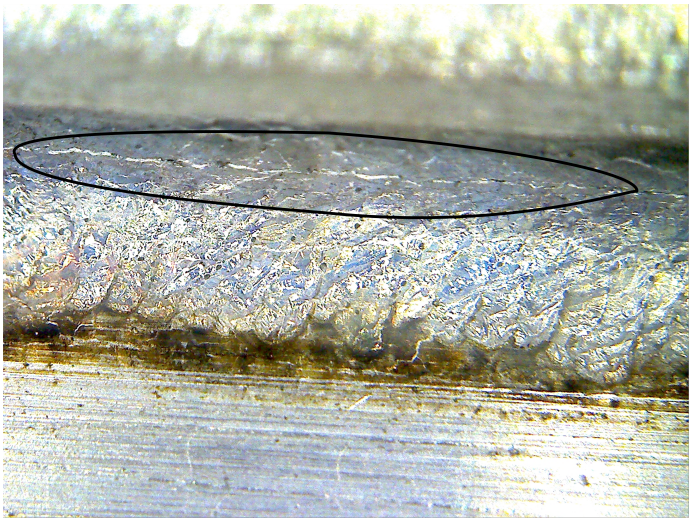

Figure E.1: Picture of 6082-6082 LBW with a large crack along the welds length.

When the 6082-6082 weld in figure E.1 was pull tested, the load bearing strength of it was well below 5 kN *(with a crude measurement and setup)* and it broke right in the crack. See figure E.2.

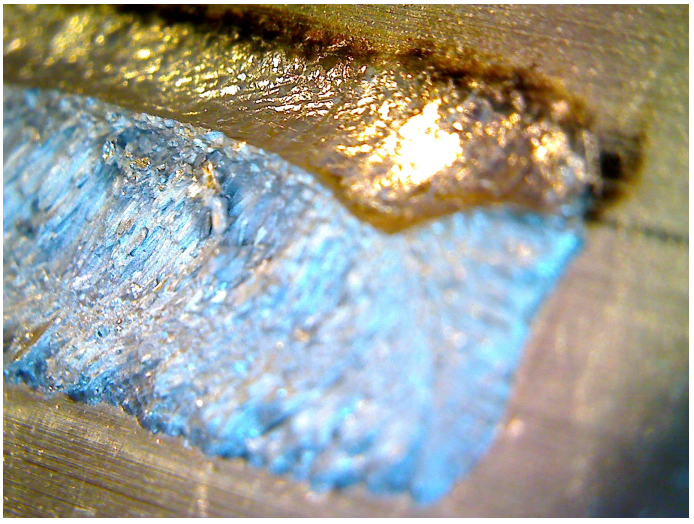

Figure E.2: Picture of 6082-6082 LBW after load failure

6082-5754

When the 6082 was welded with a sideplate of a 5754 alloy however, the load bearing stress was stopped at around 50 kN per weld. The test stopped since other parts of the jig setup started to plasticize. $b = 96mm$ and an a dimension estimated to be around $3 - 5mm$.

A picture of the 6082-5754 weld can be seen in figure E.3

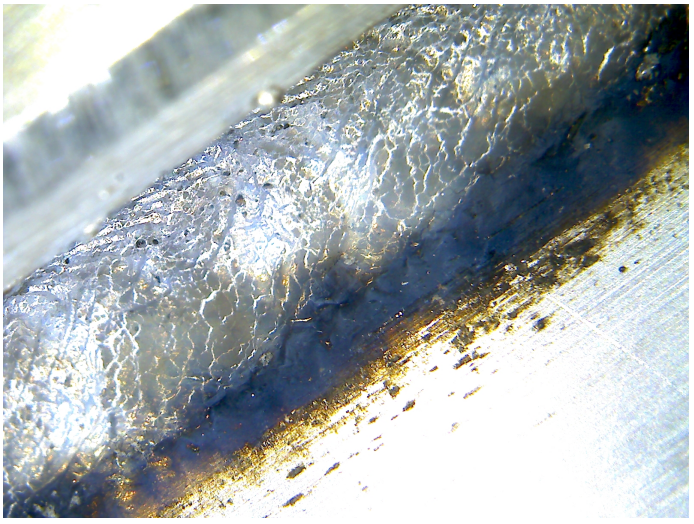

Figure E.3: Picture of 6082-5754 LBW fillet weld.

Thank you!